

# Physical interpretation of time-varying StorAge Selection functions in a model hillslope via geophysical imaging of ages of water.

Antonio Alves Meira Neto<sup>1</sup>, Minseok Kim<sup>1</sup>, and Peter A. Troch<sup>1</sup>

<sup>1</sup>University of Arizona

November 28, 2022

## Abstract

Understanding transit times (TT) and residence times (RT) distributions of water in catchments has recently received a great deal of attention in hydrologic research since it can inform about important processes relevant to the quality of water delivered by streams and landscape resilience to anthropogenic inputs. The theory of transit time distributions (TTD) is a practical framework for understanding TT of water in natural landscapes but, due to its lumped nature, it can only hint at the possible internal processes taking place in the subsurface. While allowing for the direct observation of water movement, Electrical Resistivity Imaging (ERI) can be leveraged to better understand the internal variability of water ages within the subsurface, thus enabling the investigation of the physical processes controlling the time-variability of TTD. We estimated time variable TTD through the storage selection (SAS) framework following a traditional lumped-systems approach, based on sampling of output tracer concentrations, as well as through an ERI SAS approach based on spatially distributed images of water ages. We compared the ERI-based SAS results with the output-based estimates to discuss the viability of ERI at laboratory experiments for understanding TTD. The ERI-derived images of the internal evolution of water ages were able to elucidate the internal mechanisms driving the time-variability of ages of water being discharged by the system, which was characterized by a delayed discharge of younger water starting at the highest storage level and continuing throughout the water table recession.

## Hosted file

aamn\_supporting\_information.docx available at <https://authorea.com/users/333660/articles/606820-physical-interpretation-of-time-varying-storage-selection-functions-in-a-model-hillslope-via-geophysical-imaging-of-ages-of-water>

1 **Physical interpretation of time-varying StorAge Selection functions in a model**  
2 **hillslope via geophysical imaging of ages of water.**

3

4 **Antônio Alves Meira Neto<sup>1,2\*</sup>, Minseok Kim<sup>2</sup>, and Peter A. Troch<sup>1,3</sup>**

5 <sup>1</sup>University of Arizona, Department of Hydrology and Atmospheric Sciences

6 <sup>2</sup>Institute of Climate Studies, Federal University of Espírito Santo, Vitória, ES, Brazil

7 <sup>3</sup>University of Arizona, Biosphere 2

8 \*Corresponding author: [antoniomeira@gmail.com](mailto:antoniomeira@gmail.com)

9

10

11

12

13

14 **Key points**

- 15 1. Electrical resistivity imaging was used to derive spatial distributions of water ages in a  
16 model hillslope.
- 17 2. Analysis of time-varying SAS functions indicated increasing release of younger water  
18 with decreasing storage.
- 19 3. Downward and upward soil saturation mechanisms were identified as causing the  
20 observed behavior.

21

22 **ABSTRACT**

23 Understanding transit times (TT) and residence times (RT) distributions of water in catchments  
24 has recently received a great deal of attention in hydrologic research since it can inform about  
25 important processes relevant to the quality of water delivered by streams and landscape resilience  
26 to anthropogenic inputs. The theory of transit time distributions (TTD) is a practical framework  
27 for understanding TT of water in natural landscapes but, due to its lumped nature, it can only hint  
28 at the possible internal processes taking place in the subsurface. While allowing for the direct  
29 observation of water movement, Electrical Resistivity Imaging (ERI) can be leveraged to better  
30 understand the internal variability of water ages within the subsurface, thus enabling the  
31 investigation of the physical processes controlling the time-variability of TTD. We estimated time  
32 variable TTD through the storage selection (SAS) framework following a traditional lumped-  
33 systems approach, based on sampling of output tracer concentrations, as well as through an ERI  
34 SAS approach based on spatially distributed images of water ages. We compared the ERI-based  
35 SAS results with the output-based estimates to discuss the viability of ERI at laboratory  
36 experiments for understanding TTD. The ERI-derived images of the internal evolution of water  
37 ages were able to elucidate the internal mechanisms driving the time-variability of ages of water  
38 being discharged by the system, which was characterized by a delayed discharge of younger water  
39 starting at the highest storage level and continuing throughout the water table recession.

## 40        **1. Introduction**

41    Water transit time (TT) is defined as the time spent from the moment water arrives at the land  
42    surface until it reaches the streams, a larger body of water, or is evaporated, and its estimation  
43    represents a fundamental challenge in hydrologic research. Knowledge about TT can inform a  
44    myriad of processes taking place in the subsurface, as it influences the overall equilibrium of  
45    weathering reactions (Maher, 2010, 2011) and release of nutrients (Brantley et al., 2007), while  
46    also serving as an indicator of catchment sensitivity to anthropogenic inputs (Landon et al., 2000;  
47    Turner et al., 2006).

48    The theory of transit time distributions (TTD) has been widely used as the mathematical  
49    framework to characterize TT at the catchment-scale. TTD theory considers a lumped  
50    representation of the hydrologic system, which is subject to input fluxes with known solute  
51    concentration that are modified by the TTD, yielding solute concentrations at the system's outlet.  
52    Although TTD have been traditionally studied under the assumption of steady-state conditions  
53    (Jury, 1982; Małoszewski and Zuber, 1982; Cvetkovic, 2011), surmounting evidence has been  
54    gathered towards its inadequacy to reproduce transport dynamics seen in natural landscapes, where  
55    steady-state is rarely if ever present (McGuire and McDonnell, 2006; McDonnell, 2010; Harman  
56    2015). Recent convergence towards the development of time-variable TTD has been consolidated  
57    into the theory of StorAge Selection (SAS) functions (Botter et al., 2011; van der Velde et al.,  
58    2012; Harman, 2015; Rinaldo et al., 2015; Porporato and Calabrese, 2015). Within the SAS  
59    framework, the storage within a system is considered to be composed of water parcels having  
60    varying ages. The ranked storage selection function (rSAS, Harman, 2015) is one of the existing  
61    models proposed to apply SAS theory to quantify time-variable TTD at the pedon and catchment-  
62    scale (Harman, 2015; Kim et al., 2016; Wilusz et al., 2017; Rodriguez et al., 2018). Within the  
63    rSAS framework, the age-ranked storage ( $S_T$ ) is the variable that describes the amount of storage  
64    having ages smaller than a certain value  $T$ , while the water that leaves the system at a certain  
65    moment (e.g. streamflow and evapotranspiration) is selected from storage through a storage  
66    selection function ( $\Omega_Q$ ).

67    As for the steady-state case of TTD, the estimation of the rSAS variables for real-world catchments  
68    follows an inference procedure in which information on water and solute fluxes in and out of the  
69    system is needed, together with a prior assumption of the shape of  $\Omega_Q$ . However, the direct

70 observation of time-variable TTD with no prior assumption about its shape is possible under  
71 controlled experimentation: the Periodic Tracer Hierarchy method (PERTH, Harman and Kim,  
72 2014) is a tracer experiment conceived for the direct observation of time-variable transit time  
73 distributions. The method requires a Periodic Steady State (PSS) to be imposed to the system,  
74 which allows for breakthroughs from multiple tracer injections to be quantified. Kim et al., (2016)  
75 applied the PERTH method to observe the time-variability of  $\Omega_Q$  at a  $1\text{m}^3$  sloping soil lysimeter  
76 subject to a 24-hour hydrologic cycle. They were able to verify that an inverse-storage effect (ISE)  
77 characterized the transport dynamics within the model system: under high-storage conditions,  
78 higher fractions of young water were proportionally released, whereas larger fractions of older  
79 water were released at lower storages.

80 While lumped-system approaches are useful to represent transport processes within hydrologic  
81 systems, they cannot provide spatially variable information of processes taking place within the  
82 subsurface. Therefore, additional methods that account for the internal variability of flow paths are  
83 necessary to fully investigate the temporal variability seen in natural landscapes and also promote  
84 a physical interpretation of the results arising from lumped approaches (Van der Velde et al., 2015;  
85 Rinaldo et al., 2015). Studies making use of physically based models have been proven useful to  
86 elucidate the mechanisms behind the time-variability of TTD. Ameli et al., (2016) used an  
87 integrated subsurface flow and advective-dispersive particle movement model to assess the role of  
88 subsurface architecture on flow pathways and TTD of a hillslope in Sweden. They found macro-  
89 scale heterogeneity, vertical distribution of saturated hydraulic conductivity and location of the  
90 water divide to significantly impact the structure of TTD. Yang et al., (2018) used a 3D fully  
91 coupled surface-subsurface model with random-walk particle tracking in a combined investigation  
92 of flow paths and SAS theory components from an agricultural catchment in central Germany.  
93 Their analysis suggested a shift in the age of discharged water from younger towards older when  
94 transitioning from a wet towards dry period. They found the change from fast and shallow flow  
95 paths towards deeper flow paths to explain the observed shift. Pangle et al., (2017) expanded on  
96 the results from Kim et al., (2016) by simulating the hydrologic fluxes and transport for the same  
97 experimental lysimeter through a 2D physically based model. That study suggests that the rapid  
98 mobilization of water close to the soil surface by a rising water table to result in the observed ISE.

99 The relationship between TTD variability and the underlying subsurface processes inferred  
100 through physically based modeling are however subject to modelling uncertainties and need  
101 empirical validation. Geophysical methods have been widely used to monitor tracer transport over  
102 a broad range of scales in a non-invasive way (Binley et al., 2015). Among existing geophysical  
103 methods, Electrical Resistivity Imaging (ERI) has been consolidated as a practical tool for  
104 investigating solute transport in the subsurface (Binley et al., 1996; Kemna et al., 2002; Singha  
105 and Gorelick, 2006; Koestel et al., 2008; Wehrer and Slater, 2014). Although the tracking and  
106 quantification of tracer movement through the subsurface can yield invaluable insight on water  
107 flowpaths, no study has so far used it for the direct quantification of TT.

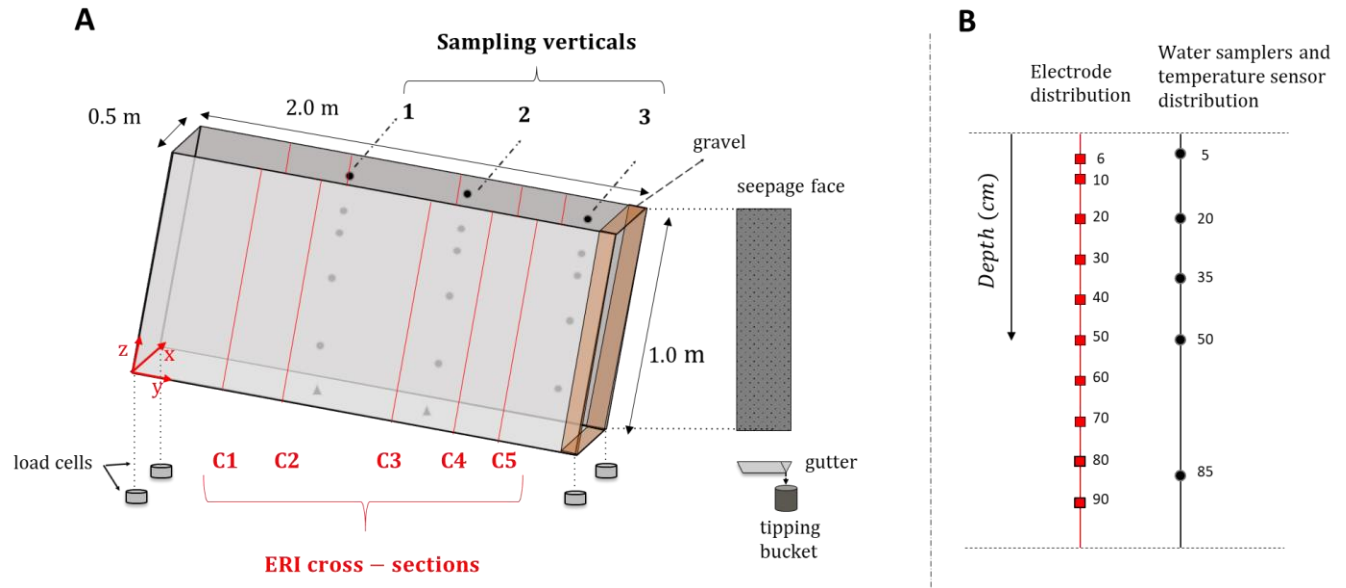
108 Here, we present an ERI-based extension of the PERTH method for the quantification of the SAS  
109 theory components at the laboratory scale. This study reports the results of the application of the  
110 PERTH method to a 1m<sup>3</sup> sloping soil lysimeter following two different approaches: 1) We  
111 estimated the rSAS components ( $S_T$  and  $\Omega_Q$ ) through a lumped approach by collecting samples of  
112 conservative tracers from irrigation and discharge, and 2) we used spatial estimates of solute  
113 concentration from ERI images to provide a spatial representation of water ages within the  
114 subsurface while also attempting to estimate ERI-derived rSAS components. With the aid of  
115 additional hydrometric data, this combined approach was leveraged to provide a physical  
116 interpretation for the lysimeter's internal functioning, and the resulting lumped estimates of  
117 transport as seen in the rSAS functions.

## 118 2. Materials and Methods

119

### 120 2.1. The MiniLEO Lysimeter

121 The miniLEO (**Figure 1-A**) is a 10-degree sloping soil lysimeter with 1m<sup>3</sup> capacity (0.5 m x 2.0 m  
122 x 1.0 m) located at the University of Arizona Biosphere 2 facility in Oracle, Arizona. The lysimeter  
123 is a small-scale replicate of the Landscape Evolution Observatory (LEO) artificial hillslopes  
124 (Pangle et al., 2015) constructed at the same facility. The interior walls and floor of the lysimeter  
125 are coated with a non-conductive abrasion-resistant waterproofing system (DuralDeck, Euclid  
126 Chemical Company). The miniLEO rests on 4 load cells (Honeywell Model 41 Load Cell) and is  
127 equipped with a sprinkler-based irrigation system composed of multiple sprinkler heads (not  
128 shown) that can be adjusted to deliver rain intensities ranging from 10 to 30 mm/h. For this  
129 experiment, the irrigation system was adjusted for a single rain intensity (14mm/h, using 3  
130 sprinkler heads) and multiple trial runs were performed to achieve a homogenous rainfall  
131 distribution over the soil surface. The lower-right end wall of the lysimeter act as a seepage face  
132 (at atmospheric pressure, no suction is applied at this boundary condition), and is composed of a  
133 perforated plastic sheet separated from the basaltic soil by a 10 cm basalt gravel layer. Seepage  
134 water is collected at a gutter and is routed to a tipping bucket (ONSET HOBO model RG3),  
135 allowing for the computation of the volumetric discharge out of the system. Discharge samples  
136 were collected at each hour throughout the course of the experiment. Vertically arranged Prenart®  
137 suction lysimeters at 5 different depths (5, 20, 35, 50 and 85 cm) are located along 3 sampling  
138 verticals (at  $y = 0.65, 1.25$  and  $1.85\text{m}$ , **Figure 1-A**). Suction lysimeters are routed to an airtight  
139 acrylic box (not shown) containing reusable plastic veils for sample collection at each  
140 corresponding location. The acrylic box is connected to a vacuum pump adjusted for -0.5 Bar  
141 suction, allowing for simultaneous sample collection from all locations. Two sensors were co-  
142 located with the suction lysimeters (with an approximate separation of 5 cm in the x-direction):  
143 Decagon® MPS-2 matric potential sensors, used to provide temperature readings, and Decagon®  
144 5TM for measurements of volumetric soil water content. Additionally, two Campbell CS451  
145 pressure transducers were installed at the lysimeter floor (triangles in **Figure 1-A**).



146

147 **Figure 1. Schematic view of the miniLEO soil lysimeter. A- Overview of the lysimeters dimensions, sampler**  
 148 **and sensor locations, ERI verticals (red lines) along the walls and overall instrumentation. ERI measurements**  
 149 **were taken at verticals from opposite sides of the lysimeter, producing cross-sectional images (cross-sections**  
 150 **C1 through C5). Triangles represent Campbell CS451 pressure transducers. The Coordinate system (x, y and**  
 151 **z directions) used throughout the text is highlighted in the lower end of the lysimeter. The location of the vertical**  
 152 **gravel layer is shown in brown. Aside from this layer, the lysimeters volume was filled with the basaltic loamy**  
 153 **sand. A metallic structure (not shown here) responsible for supporting the lysimeters weight and keeping it at**  
 154 **a 10° angle did not allow for a uniform distribution of ERT verticals along the y-axis. B- Depth distribution of**  
 155 **stainless-steel electrodes (red) and water samplers (Prenart ® suction lysimeters – black circles).**

156 The material within the miniLEO is a basalt tephra extracted from a deposit in northern Arizona  
 157 that was further ground on site to a loamy sand texture. The final texture distribution was achieved  
 158 by sieving and remixing different size fractions of the original basalt so that a larger percentage of  
 159 fines could be achieved (Dontsova et al., 2009). This procedure led to a final texture consisting of  
 160 approximately 85% sand-size particles ( $\geq 50$  and  $< 2000 \mu\text{m}$ ), 12% silt-size particles ( $\geq 2$  and  
 161  $< 50 \mu\text{m}$ ), and 3% clay-size particles ( $< 2 \mu\text{m}$ ). The material, herein referred to as basaltic soil, is the  
 162 same as in the LEO hillslopes and was chosen as part of the investigation of the coevolution of  
 163 soils and landscape complexity mediated by physical and biogeochemical processes (Pangle et al.,  
 164 2015). The intended low content of fine particles (approx.  $32 \text{ g kg}^{-1}$ ) should allow for an easier  
 165 detection of incipient secondary mineral formation (Pohlman et al., 2016). Even though clay-sized  
 166 particles are present in the basaltic soil, no secondary minerals were observed as part of the basalt's  
 167 mineralogical composition (Dontsova et al., 2009; Pangle et al., 2015; Pohlman et al., 2016). The

168 basaltic soil was added to the lysimeter through a procedure consisting of sequentially adding 32  
 169 cm increments of loose soil, which were then compacted to 25cm. During this procedure, the first  
 170 10 centimeter from the seepage face were occupied by the original gravel-size basaltic tephra to  
 171 serve as a drainage layer.

172 10 ERI verticals (located at  $y = 0.25, 0.55, 1.1, 1.4,$  and  $1.63$ ) containing 10 electrodes each are  
 173 distributed along both walls of the lysimeter, as seen in **Figure1-A** and **B**. The location of the ERI-  
 174 verticals was chosen in order to avoid overlap with sensor-verticals and also due to inaccessibility  
 175 of certain portions of the lysimeter wall that were blocked by the metal structure used to keep the  
 176 lysimeter at its 10-degree slope (see **Figure S1-A** for more details). This layout allows for  
 177 acquisition of 5 cross-sectional resistivity images at different locations along the y-direction,  
 178 hereafter referred to as cross-sections C1 through C5, in which the number 1 represents the upper  
 179 most cross-section ( $y = 0.25$  m) and 5 the lower most ( $y = 1.63$  m). The electrode distribution of  
 180 each vertical follows a 10 cm spacing interval, with the exception of the first electrode position  
 181 (**Figure1-B**). The electrodes are 3 mm diameter stainless steel rods secured by plastic cable glands  
 182 installed through orifices in the lysimeter walls. The electrodes were installed prior to the soil  
 183 packing and the orifices were sealed with the same non-conductive water-proofing system used  
 184 internally (see **Figure S1-B** for more details).

## 185 2.2. rSAS Theory

186 The ranked storage selection theory (rSAS) is one of the existing variations within the SAS  
 187 framework (Botter et al., 2011; Rinaldo et al., 2015; van der Velde et al., 2012). In this theory, the  
 188 system is assumed to be a single control volume, subject to a precipitation  $J(t)$  input flux and the  
 189 output fluxes from discharge  $Q(t)$  and evapotranspiration  $ET(t)$ . At any moment  $t$ , the ages ( $\mathcal{T}$ )  
 190 of water in storage can be represented by the residence time distribution  $P_S(\mathcal{T}, t)$ , representing the  
 191 cumulative distribution of ages within the system. The fluxes in and out of the system will alter  
 192 the structure of  $P_S(\mathcal{T}, t)$  over time, through the cumulative backwards transit times distributions  
 193 (bTTD) of discharge  $\overline{P}_Q(\mathcal{T}, t)$  and evapotranspiration  $\overline{P}_{ET}(\mathcal{T}, t)$ . We can write the continuity  
 194 equation of ages and mass within the system as (Harman et al., 2015):

$$195 \quad \frac{\partial S_T(\mathcal{T}, t)}{\partial t} = J(t) - Q(t)\overline{P}_Q(\mathcal{T}, t) - ET(t)\overline{P}_{ET}(\mathcal{T}, t) - \frac{\partial S_T(\mathcal{T}, t)}{\partial \mathcal{T}}, \quad (1)$$

196 where the age-ranked storage,  $S_T(\mathcal{T}, t)$  represents the actual storage having ages  $\mathcal{T} < T$ :

$$197 \quad S_T(T, t) = S(t)P_S(T, t) \quad (2)$$

198 where  $S(t)$  represents storage, in mm. Equation 1 shows that  $S_T$  is modified in time by the  
 199 increase in storage from precipitation (assumed to have age equal to zero), the decrease in  
 200 storage with age selection being determined from  $\overline{P_Q}(T, t)$  and  $\overline{P_{ET}}(T, t)$  and the ageing of  
 201 water within the system as  $\frac{\partial S_T(T, t)}{\partial T}$ . While difficult to parameterize, the terms  $\overline{P_Q}(T, t)$  and  
 202  $\overline{P_{ET}}(T, t)$  have been found to be more conveniently expressed as cumulative functions of  $S_T$ :

$$203 \quad \Omega_Q(S_T, t) = \overline{P_Q}(T, t) \quad (3)$$

$$204 \quad \Omega_{ET}(S_T, t) = \overline{P_{ET}}(T, t) \quad (4)$$

205 where  $\Omega_Q$  and  $\Omega_{ET}$  are the rSAS functions of discharge and evapotranspiration. The rSAS  
 206 functions therefore represent the outflux selection from the age-ranked storage, and the  
 207 transformation from  $P(T, t)$  to  $\Omega(S_T, t)$  is possible due to the direct mapping between  $T$  and  
 208  $S_T$ . We assume the soil evaporation throughout the experiment to be negligible, as we  
 209 attempted to keep such flux at a minimum by shutting off air circulation fans, and keeping the  
 210 air inside the facility at a reasonably high relative humidity values. Such assumption was  
 211 similarly taken in the studies from Kim et al., (2016, 2020), performed in the same facility, for  
 212 which meaningful estimates of the SAS components were still obtained.

213

### 214 **2.3. PERTH Experiment and Retrieved rSAS Components.**

215 The experiment is an application of the Periodic Tracer Hierarchy (PERTH) method (Harman  
 216 and Kim, 2014), conceived for the direct observation of time-varying transit time distributions.  
 217 A short description of the method is provided here, and a more in-depth discussion of the  
 218 method can be found in Kim et al. (2021).

219 Through the PERTH method, it is possible to quantitatively separate overlapping (in time)  
 220 breakthrough curves resulting from repetitive injections of the same tracer. Breakthrough  
 221 curves from each injection are assumed to result from an instantaneous injection of a  
 222 conservative tracer, providing realizations of the forward transit time distribution (fTTD, aka  
 223 system response function) (Niemi, 1977). For a system that is not in steady state, that  
 224 realization of the fTTD would be conditional on the time of injection  $t_i$ , as indicated in the

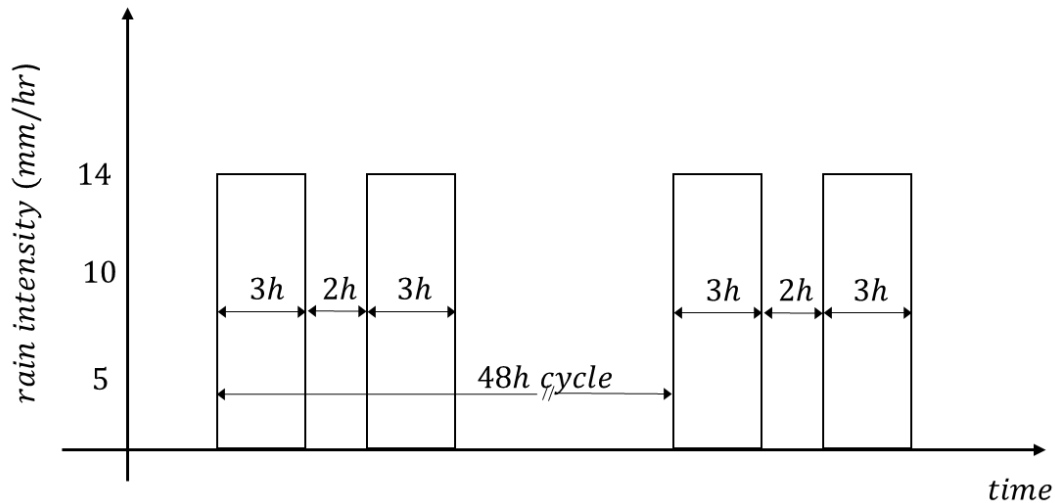
225 notation commonly used for this probability distribution:  $\vec{p}(t - t_i | t_i)$ . By repeated injections  
226 of the same tracer in a system under unsteady-state conditions, additional realizations of the  
227 fTTD are obtained, with each of them being uniquely affected by the hydrological conditions  
228 that existed at the time of injection  $t_i$ , and thereafter. Although this can lead to a direct  
229 quantification of the time dependence of fTTDs, the time necessary for its execution would  
230 make it infeasible, since for each injection we would require complete flushing of the tracer.  
231 The PERTH method makes it possible to directly observe time-variable fTTDs over a much  
232 shorter experimental period.

233 For the application of the PERTH method, a periodic steady state (PSS) condition (Harman  
234 and Kim, 2014) is required, which can be achieved by the application of an irrigation cycle  
235 that is systematically repeated. Under PSS conditions, the system will be forced to repeat the  
236 same internal states (total storage and spatial moisture content distribution) and outputs  
237 (discharge through the outlet). The PERTH method consists in the sequential injection of  
238 different tracers while the system is experiencing PSS conditions and its final goal is the  
239 estimation of the time-variability of rSAS components within one cycle.

240 In this study, the PSS experiment was conducted between June 22<sup>nd</sup> and July 21<sup>st</sup> 2018 and  
241 consisted of the repetition of an irrigation schedule within 48 hour cycles ( $t_c = 48$  h, following  
242 the notation of Harman and Kim, (2014)). Each cycle consisted of two 3-hour-long irrigation  
243 pulses separated by a 2-hour period, both having a target intensity of 14 mm/hr. The pulses  
244 were applied from 8:30 to 11:30 and from 13:30 to 16:30 of the first day, while no irrigation  
245 occurred during the second day (**Figure 2**). Seven irrigation cycles occurred before the  
246 introduction of tracers in order to bring the system to a PSS.

247 We used chloride (dissolved LiCl in irrigation water), as a reference tracer ( $C_R$ ) and deuterium  
248 ( $^2\text{H}$ ) and oxygen-18 ( $^{18}\text{O}$ ) as probe tracers ( $C_0$  and  $C_1$ , respectively). A whole cycle with tracer-  
249 labeled water was applied once PSS was achieved: The first pulse was labeled with  $C_R$  and  $C_0$ ,  
250 while the second pulse contained  $C_R$  and  $C_1$ . A value of 10000  $\mu\text{mol/L}$  of chloride was chosen  
251 for  $C_R$  (reference tracer), while the values of  $\delta^2\text{H}$  and  $\delta^{18}\text{O}$  of 250 ‰ and 15 ‰ (VSMOW)  
252 were selected for  $C_0$  and  $C_1$  (probe tracers) respectively. Discharge water samples were  
253 collected hourly and analyzed for  $\delta^2\text{H}$  and  $\delta^{18}\text{O}$  relative to Vienna Standard Mean Ocean  
254 Water (VSMOW) using a Los Gatos Research DLT-100 Laser Spectrometer. We obtained

255 chloride concentrations from electrical conductivity measurements of discharge water samples  
 256 using a linear relationship calibrated in the laboratory ( $r^2 = 0.99$ ) relating chloride  
 257 concentration to electrical conductivity. Following the tracer application, additional irrigation  
 258 cycles were scheduled until water samples at the sampling locations reached pre-injection  
 259 conductivity values.  
 260



261  
 262 **Figure 2. Schematic of the 48 hours cycle of rain application imposed at the miniLEO lysimeter.**

263

#### 264 **2.4. ERI-based Estimation of Internal Ages of Water and rSAS Components**

265 We estimated the internal distribution of ages of water within one PSS cycle by converting ERI-  
 266 based images of soil bulk electrical conductivity ( $\sigma_b$ , in  $\mu S/cm$ ) into images of fluid conductivity  
 267 ( $\sigma_f$ , in  $\mu S/cm$ ) which were then converted to Cl concentration ( $\frac{\mu mol}{L}$ ). The ERI surveys produced  
 268 cross-sectional images at the 5 y-direction locations of the ERI verticals (i.e. 2D panels across the  
 269 x-z dimensions, **Figure 1A**), which were extrapolated to produce lysimeter-wide panels (2D panels  
 270 across y-z dimensions, **Figure 1A**).

271 A more detailed description of the ERI application is presented in the following sections. In  
 272 **Section 2.4.1** we provide details on the acquisition, pre-processing and inversion of ERI data.  
 273 **Section 2.4.2** elaborates on the procedure to extract images of estimated  $\sigma_f$  across the soil  
 274 lysimeter and its conversion into Cl concentration images across the lysimeters length. Finally,

275 **Section 2.4.3** describes how the estimated Cl concentrations were converted into images of water  
276 ages across one representative PSS cycle.

#### 277 **2.4.1. Collection, Preprocessing and Inversion of ERI Data.**

278 Measurements of soil resistance ( $R$  –ratio of measured voltage between a pair of electrodes by the  
279 current injected between another pair or electrodes) were performed using the 8 channel Supersting  
280 R8 (Advanced Geosciences Inc.) electric resistivity meter. We followed a time-lapse cross-  
281 borehole survey designed to obtain 2D cross-sectional images at the 5 locations along the y-  
282 direction. 2D cross-borehole configurations allow for quick image acquisition and have been  
283 widely used for studies of solute transport and plume migration in a variety of environments (Slater  
284 et al., 2000; Kemna et al., 2002; Looms et al., 2008; Perri et al., 2012; Bellmunt et al., 2016). A  
285 skip-dipole (Slater et al., 2000) measurement scheme with 2 and 3 electrode distances as the  
286 assigned skip, representing 248 measurements to be taken per cross-section (including reciprocals)  
287 was chosen. A survey consisted of repeating the same scheme from cross-sections 1 through 5,  
288 resulting in a total of 1240 measurements per run. A total of 1190 surveys were performed between  
289 June 22<sup>nd</sup>, 2018, and July 21<sup>st</sup> 2018, with each survey taking approximately 35 minutes. Poor soil-  
290 electrode contact during dry days allied to the low-conductivity water used in the rain pulses made  
291 it impossible for all readings to be taken at all surveys. This led to a reduction of the total  
292 measurements to an average of 1182 per survey (237 measurements per cross section, in average).

293 An error analysis procedure was conducted prior to the inversion. We first excluded obvious  
294 outliers by removing measurements with reciprocal error ( $\epsilon_{recip}$ , Slater et al., 2001) greater than  
295 5%, which resulted in a 7% reduction of the initial number of measurements. Following that, we  
296 estimated an error model for each survey in order to estimate weights to be used in the inversion  
297 (Slater et al. 2001, Koestel et al., 2008, Wehrer and Slater, 2015). This was done by binning the  
298 reciprocal measurement ( $\bar{R}$ ) values in 10 classes with increasing order of magnitude and fitting a  
299 linear relationship between binned values of  $\bar{R}$  and  $\epsilon_{recip}$ , from which the slope and intercept were  
300 retained.

301 The surveys were inverted with the code R3t (Binley, 2013), which estimates the spatial  
302 distribution of resistivities from measured potential and current values. We used the software  
303 Gmsh (Geuzaine and Remacle, 2009) to generate a three-dimensional finite element mesh  
304 consisting of 20640 tetrahedral elements with characteristic length of 5 cm. A time-lapse ERI

305 inversion scheme based on the difference regularization method of Labrecque and Yang (2001)  
 306 was used in this study. This method allows for faster convergence and tends to minimize systematic  
 307 errors. First, a reference dataset to be used as the a priori model for subsequent inversions is  
 308 inverted according to the following objective function:

$$309 \quad \Psi_d = (W_d[\mathbf{d} - f(\mathbf{m})])^2 + \alpha(W_m \mathbf{m})^2, \quad (5)$$

310 Where  $\mathbf{d}$  is the vector of measured resistances (*Ohm*),  $\mathbf{m}$  is the model vector of resistivities  
 311 (*Ohm.m*),  $f(\mathbf{m})$  is the forward solution of the resistances,  $W_d$  is a matrix containing the data  
 312 weights,  $W_m$  is the roughness matrix, which is used to generate a smooth solution by penalizing  
 313 differences between adjacent values of modelled resistivities and  $\alpha$  is a smoothing parameter,  
 314 which assigns a weight to the second term of the objective function. The first term of the objective  
 315 function represents the misfit between modelled and measured data, while the second is a measure  
 316 of smoothness of the forward model. After the reference dataset is inverted, the data vector ( $\mathbf{d}$ ) is  
 317 modified for the subsequent datasets as:

$$318 \quad \mathbf{d} = \mathbf{d}' - \mathbf{d}_{ref} + f(\mathbf{m}_{ref}) \quad (6)$$

319 Where  $\mathbf{d}'$  is the vector of measured resistances at a subsequent time,  $\mathbf{d}_{ref}$  represents the measured  
 320 resistances used in the reference dataset and  $f(\mathbf{m}_{ref})$  is the forward solution of the reference  
 321 dataset. A new objective function based on the minimization of the differences between current  
 322 and reference datasets and the smoothness term is then calculated:

$$323 \quad \Psi_d = (W_d[\mathbf{d} - f(\mathbf{m})])^2 + \alpha(W_m[\mathbf{m} - \mathbf{m}_{ref}])^2, \quad (7)$$

324 Two-dimensional cross-sectional images of bulk resistivity were extracted from the inverted three-  
 325 dimensional fields of resistivities and further converted to bulk conductivity values ( $\sigma_b, \mu S/cm$ ).  
 326 Since electrical conductivity is influenced by temperature (Campbell et al., 1948), the resulting  
 327 conductivity values were corrected to a reference temperature by:

$$328 \quad \sigma_b(T_{ref}) = \frac{\sigma_b(T)}{1 + 0.02(T - T_{ref})} \quad (8)$$

329 Where  $T$  is the in-situ temperature provided by the MPS2-2 matric potential sensors (see Section  
 330 2.1), and  $T_{ref}$  is a reference temperature (25 °C). Measurements from the co-located temperature

331 sensors were spatially interpolated and extrapolated to generate spatial temperature estimates at  
 332 the cross-sections at the different times.

#### 333 **2.4.2. Spatial and Temporal Estimates of Cl Concentration**

334 The petrophysical relationships between soil bulk electrical conductivity/resistivity and its  
 335 controlling variables differ for soils with and without clay minerals. The formulations presented  
 336 in this section provide a method for using the PSS imposed throughout the PERTH experiment to  
 337 extract the fluid conductivity assuming a soil with negligible clay formation, as is the case for the  
 338 basaltic soil inside the miniLEO. A slightly modified experimental procedure can be executed in  
 339 the case of soils with clay minerals, and its description is provided as supporting information (**Text**  
 340 **S1**).

341 For non-conductive soils, the soil bulk electrical conductivity ( $\sigma_b$ , in  $\mu S/cm$ ) can be explained as  
 342 a function of the conductivity of the soil water ( $\sigma_f$ ), porosity ( $\phi$ ) and water-saturation ( $S$ ), and is  
 343 described by Archie's law (Archie, 1942) as:

$$344 \quad \sigma_b = \sigma_f \phi^m S^n \quad (9)$$

345 where  $m$  is the cementation exponent, and  $n$  is the saturation exponent. It can be seen that  $\sigma_b$   
 346 estimated through ERI surveys are controlled by multiple variables. In order to convert the  
 347 estimates of  $\sigma_b$  into fluid conductivity ( $\sigma_f$ ), estimates of soil porosity ( $\phi$ ), water saturation ( $S$ ),  
 348 and eventually soil-surface conductivity ( $\sigma_s$ ) are needed. This poses additional challenges for the  
 349 quantitative assessment of solute transport through ERI methods. These circumstances limit ERI  
 350 applications to steady-state conditions when the exponents  $m$  and  $n$  are unknown (Binley et al.,  
 351 1996; Slater, 2001; Alumbaugh et al., 2004; Koestel et al., 2008), or will require the knowledge of  
 352 both soil parameters and moisture states through time for unsteady-state conditions (Wehrer and  
 353 Slater, 2015).

354 A simple approach that takes advantage of the repeatability seen at PSS conditions can be  
 355 developed that allows for a quantitative characterization of solute transport under unsteady state  
 356 conditions with spatially varying degrees of saturation. Under PSS, the variables in equation 9  
 357 become a function of the time relative to the beginning of a cycle ( $t^*$ ):

$$358 \quad \sigma_b(t^*) = \sigma_f(t^*) \phi^m S(t^*)^n. \quad (10)$$

359 The internal states and outputs achieved within a PSS-cycle will result from an interplay between  
 360 internal properties (porosity, hydraulic conductivity, and retention characteristics) and the input  
 361 sequence. Considering a soil lysimeter subject to an irrigation schedule, moisture states and fluxes  
 362 can vary from saturated to unsaturated conditions both in space and time depending on the intensity  
 363 and duration of the imposed irrigation sequence.

364 Assuming that PSS conditions have been achieved, and that water with known background tracer  
 365 concentrations and conductivity has been used, the system will be in what we define as a “warmup”  
 366 ( $w$ ) period. The response of a warmup cycle as:

$$367 \quad \sigma_b(t_w^*) = \sigma_f(t_w^*)\phi^m S(t_w^*)^n, \quad (11)$$

368 where  $t_w^*$  is the time relative to the beginning of the warmup cycle. Once PSS is reached, the  
 369 progression  $\sigma_b$  within a cycle should be repeated at every cycle. The estimation of a representative  
 370 warmup cycle can therefore be taken from any cycle within PSS conditions, or an average of all  
 371 warmup cycles to account for between cycle variability that can potentially arise due to failure in  
 372 repeating the exact input sequence. Following that, an “injection” cycle can be performed, in which  
 373 water with contrasting concentrations (and conductivity) is applied. Subsequent cycles are then  
 374 imposed with the previously used background concentrations until tracer recovery is satisfactorily  
 375 achieved. For the cycles from injection until the end of recovery the soil-bulk conductivity can be  
 376 written as:

$$377 \quad \sigma_b(t_k^*) = \sigma_f(t_k^*)\phi^m S(t_k^*)^n \quad (12)$$

378 where  $t_k^*$  is the time relative to the beginning of the  $k^{th}$  cycle ( $k = 1$  representing the injection  
 379 cycle). By dividing each injection or recovery cycles response by the warmup-cycle response, the  
 380 following expression can be written:

$$381 \quad \frac{\sigma_b(t_k^*)}{\sigma_b(t_w^*)} = \frac{\sigma_f(t_k^*)}{\sigma_f(t_w^*)} \cdot \frac{\phi^m S(t_k^*)^n}{\phi^m S(t_w^*)^n}, \quad (13)$$

382 Since the term  $\phi^m S(t)^n$  is the same for all cycles, we arrive at:

$$383 \quad \sigma_{rat}(t_k^*) = \frac{\sigma_b(t_k^*)}{\sigma_b(t_w^*)} = \frac{\sigma_f(t_k^*)}{\sigma_f(t_w^*)} \quad (14)$$

384 where  $\sigma_{rat}$  is the ratio between bulk conductivities from injection or recovery cycles and that of  
 385 the warmup cycle. Assuming that the pore-water conductivity throughout a warmup cycle,  $\sigma_f(t_w^*)$ ,  
 386 can be estimated, equation 14 provides a solution for  $\sigma_f$  at any arbitrary time  $t$ .

387 ERI-based values of concentration ( $C_{Cl}$ ) were obtained by converting  $\sigma_f$  into values of  
 388 concentration using a relationship between chloride concentration ( $\mu mol/L$ ) and electrical  
 389 conductivity ( $\mu S/cm$ ) from soil-water samples using a linear relationship calibrated in the  
 390 laboratory ( $r^2 = 0.99$ ). We produced depth-averaged profiles of  $C_{Cl}$  at 10-cm spacing for visual  
 391 assessment of chloride breakthroughs. For evaluation of the results, values of  $C_{Cl,obs}$  from the 3  
 392 water sampling verticals were superimposed onto the ERI-cross sections by linear interpolation,  
 393 while  $C_{Cl}$  values were averaged at the equivalent locations. Details on depth-profile evaluation of  
 394 the results are presented as supporting information (**Text S2, Figures S2 and S3, Table S1**).

395 Finally, 2-dimensional (along the y-z direction) panels of chloride concentration starting from the  
 396 injection cycle and onwards were created based on the spatial interpolation of depth averaged  
 397 profiles across the ERI-domain. Following that, warmup-cycle field of conductivities, spatially  
 398 interpolated from the suction cups were subtracted from the injection and recovery cycle panels to  
 399 yield a final sequence of Cl-breakthrough panels.

#### 400 **2.4.3. Ages of Water within a PSS Cycle**

401 We estimated the spatial distribution of water ages within one PSS cycle using the spatial  
 402 distributions of solute concentration from the tracer injection and subsequent irrigation cycles. For  
 403 each time-step  $t$ , with  $t = 0$  being the moment of the injection, the observed fraction of water from  
 404 the injection was estimated as:

$$405 \quad f_t = \frac{C_{Cl}(t)}{C_{In}}, \quad (15)$$

406 where  $C_{In}$  is the concentration of the injected tracer. Since the moment of each image is known,  $f_t$   
 407 can be interpreted as the fraction of water having age equal to  $t$ . This resulted in estimates of  $f_t$   
 408 throughout 8 irrigation cycles (cycles 8 through 15 as seen in **Figure 3**), leading to observed  
 409 fractions of water with ages up to 384 hours (8 cycles times 48 hours per cycle).

410 The PSS conditions imposed on the system implies that each irrigation pulse will lead to the same  
 411 internal response, allowing for the assumption that the tracer progression observed since the

412 injection cycle will be the same for each subsequent non-tracer-labelled cycle. Therefore, the last  
 413 cycle will contain water having ages from the time of the injection up to the maximum observable  
 414 age, in this case, 384 hours. We refer the last cycle hereinafter as the *representative cycle*. Since  
 415 the chloride tracer was added throughout 2 pulses, the determination of the ages during the-  
 416 injection period (ages from 1 to 8 hours) was not possible. Therefore, we assigned an average age  
 417 of 4 hours for the water being injected during first 8 hours of the experiment.

418 The superposition of sequential tracer injections leads to the possibility for a point within the  
 419 domain to be assigned different values of  $f_t$ . That occurs due to two main reasons: (i) the same  
 420 point might contain some remaining fraction of water from a previous irrigation event when water  
 421 from a new irrigation event is applied, and (ii) the ERI estimation of chloride concentration are  
 422 subject to a smoothness arising from the inversion procedure. Therefore, at any specific moment  
 423 within the representative PSS cycle, a single location might have water with varying ages. For the  
 424 visual assessment of the spatial distribution of water ages within a representative cycle, we  
 425 assigned for each pixel the age  $\mathcal{T}^*$ , representing the most frequent age (i.e., the age  $\mathcal{T}$  with the  
 426 higher  $f_t$ ).

#### 427 **2.4.4. ERI-Based Estimation of SAS Theory Components**

428 Once the internal distribution of ages within the representative PSS cycle was obtained, we  
 429 followed with the estimation of the age-ranked storage ( $S_T$ ). As noted previously,  $S_T$  represents  
 430 the volume of water that has age less than or equal to  $T$ , with  $T$  being the time spent from the  
 431 moment of entry up to the current time  $t$ . We combined the interpolated images of soil water  
 432 content from the in-situ sensors with those of  $f_t$  for each moment  $t$ . We first estimated the age  
 433 ranked-storage density  $s_T(\mathcal{T}, t)$ , by calculating at each pixel the product between storage and the  
 434 fraction of water having age  $\mathcal{T}$ :

$$435 \quad s_T(\mathcal{T}, t) = \sum v_{i,t} \cdot f_{t=\mathcal{T}}, \quad (16)$$

436 Where  $v_i$  is the volume of storage of a pixel  $i$  (mm),  $t$  is the time within the representative cycle  
 437 (1 through 48), and  $f_{\mathcal{T},t}$  is the assigned fraction of water having the age  $\mathcal{T}$  at the same moment.  
 438  $v_i$  was estimated as the product of the volumetric water content at a pixel and its storage capacity  
 439 (mm). We followed by estimating  $S_T$  as:

440 
$$S_T^*(\mathcal{J}, t) = \sum_{a=0}^{\mathcal{J}} s_T(a, t) \quad (17)$$

441 where the \* symbol denotes ERI-based estimate. Following that, we estimated the storage selection  
 442 function ( $\Omega_{Q^*}$ ) by first calculating the cumulative sum of the differences between the  $s_T(\mathcal{J}, t)$   
 443 vectors from each time-step, normalized by the change in storage between time-steps:

444 
$$\Omega_{Q^*}(S_T^*(T, t), t) = -\frac{S_T^*(T, t + \Delta t) - S_T^*(T - \Delta T, t)}{\Delta t} / Q^* \quad (18)$$

445 Where  $Q^*$  represents the total change in storage within the ERI surveyed domain over time,  
 446 computed as:

447 
$$Q^* = \frac{\sum v_{i,t+1} - \sum v_{i,t}}{\Delta t} \quad (19)$$

448 **3. RESULTS**

449

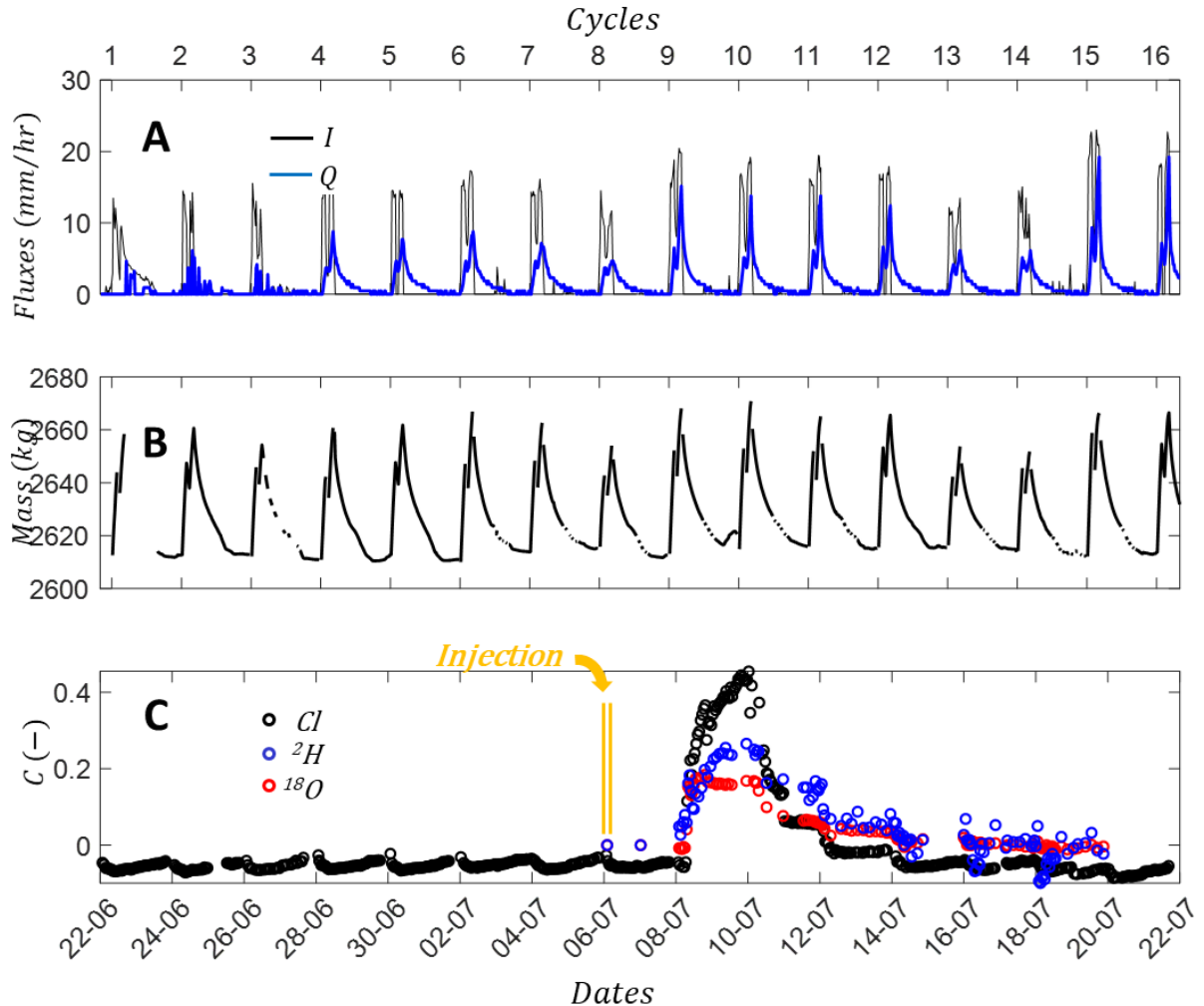
450 **3.1. Hydrologic Assessment of the Experiment**

451 The overall progression of the experiment can be seen in **Figure 3**. Seven warmup cycles occurred  
452 prior to the injection (8<sup>th</sup> cycle), followed by another 8 recovery cycles. **Figure 3A** shows the  
453 irrigation intensity ( $I$ ) applied through the several pulses as well as measured seepage-face  
454 discharge ( $Q$ ), whereas the load-cell mass changes are shown in **Figure 3B**. The estimated mean  
455 rainfall intensity was 13 mm/hr per pulse, with a standard deviation of 3 mm/hr (Coefficient of  
456 variance of 23%). Such variability occurred due to malfunctioning of the micro-controller that  
457 adjusts the pressure at the inlet of the tubing system that distributes water to the sprinklers. The  
458 resulting spatial distribution resulted in higher intensities closer to the seepage face, where the  
459 average intensity at the upper third was approximately 10 mm/hr, followed by 12 and 15 mm/hr at  
460 middle-slope and seepage face thirds respectively. Even though the system quickly reached an  
461 oscillatory pattern from cycle #1, as seen in the variations in mass (**Figure 3B**), additional cycles  
462 were performed due to the issues mentioned previously. Electrical issues within the data-logging  
463 system during the cycles 1 and 3 led to poor estimation of mass and discharge values.

464

465 **Figure 3C** shows the tracer breakthroughs for chloride,  $^2\text{H}$  and  $^{18}\text{O}$  (“C), taken concentrations  
466 normalized by their injection and background values. The two irrigation pulses containing the  
467 tracers as described in **2.3** are depicted as two vertical yellow bars (not in scale, simply for  
468 illustration of the moments of the injection). A delayed tracer response can also be identified where  
469 the discharge conductivity is seen to increase after the first cycle of the recovery period (Cycle 9,  
470 day 2 in **Figure 3C**). It is also possible to see that both  $^2\text{H}$  and  $^{18}\text{O}$  were not detected in the same  
471 quantities as chloride, suggesting an imperfect tracer recovery of both tracers when compared to  
472 chloride. We were not able to define the actual cause for this issue, but a possible reason could  
473 have been an incorrect amount of tracer added to the irrigation system.

474



475

476

477 **Figure 3. Hydrologic progress of the miniLEO lysimeter under a periodic steady state throughout the**  
 478 **experiment. A- Irrigation (mm/hr) sequence applied throughout the experiment (black) and discharge (mm/hr)**  
 479 **from the lysimeters seepage face (blue). B- Mass variations (kg) registered through the load cells indicate the**  
 480 **increase in mass due to irrigation pulses and drainage periods. Equipment failure during the cycles 1 and 3**  
 481 **were responsible for missing values of mass and poor estimates of discharge for those periods. C- Normalized**  
 482 **Concentrations for discharge fluxes.**

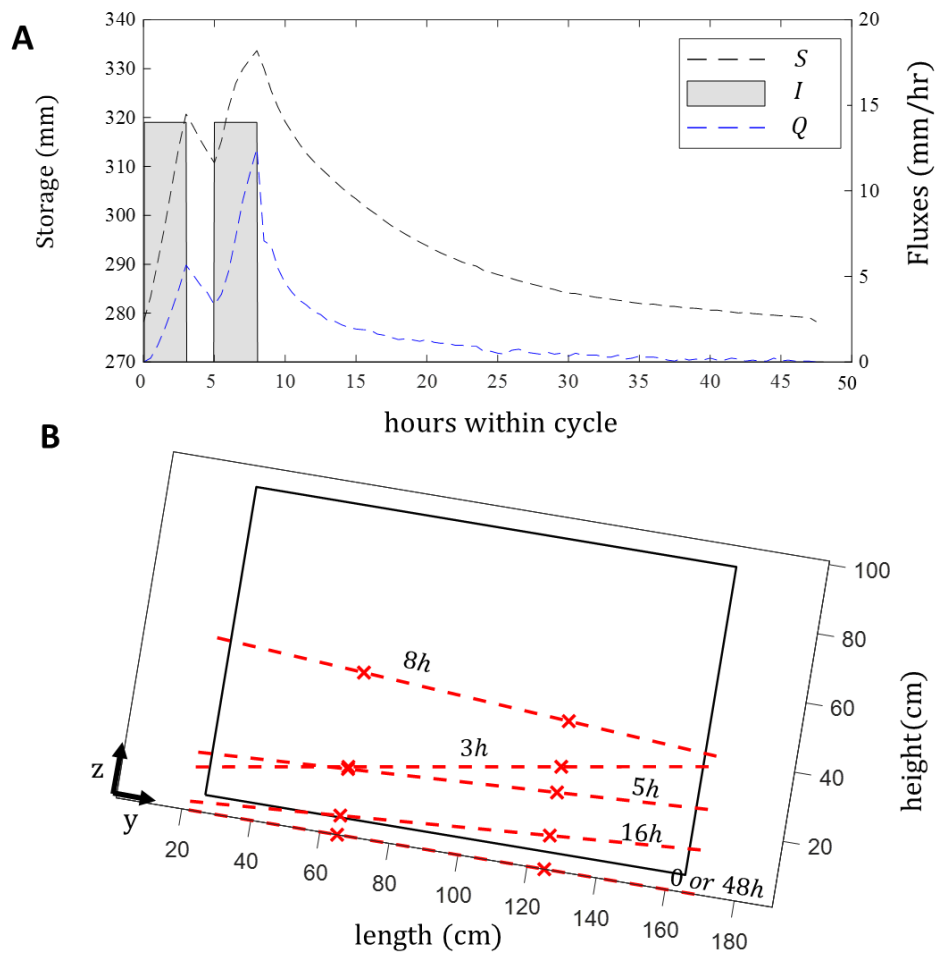
483

484 Additional insights on the hydrologic processes within a cycle can be gained by analyzing both  
 485 external and internal responses. **Figure 4A** shows the average responses of irrigation, discharge,  
 486 and storage within the 48-hour cycle. It is possible to see the double peaked response in storage  
 487 and discharge resulting from the sequential irrigation pulses, followed by a recession period.  
 488 **Figure 4B** shows the approximate water table location at the instants 3, 5, 8, 16 and 48h. The water

489 tables were obtained by linearly interpolating the observed values from the two pressure  
 490 transducers (**Figure 1A**). While initially absent, the water table rises to a first peak at  $t = 3h$ ,  
 491 followed by a quick recession due to the absence of rainfall between  $t = 3h$  and  $t = 5h$ . With the  
 492 end of the second irrigation pulse, the water table reaches its second peak at  $t = 8h$ , which is  
 493 followed by a recession (see  $t = 16h$ ) and the absence of a water table characterizing the initial  
 494 conditions of the cycle.

495

496



497

498

499 **Figure 4. Characteristic (average) hydrologic responses within one cycle. A - Sequence of two 2-hour long**  
 500 **irrigation pulses (gray bars) separated by a 2-hour period resulting in increasing storage (black dashed line)**  
 501 **and discharge (blue dashed line), followed by a recession period. B - Approximate location of the water table**

502 measured by pressure transducers (red x symbols), linearly interpolated throughout the ERI domain (inner  
503 square).

504

## 505 3.2. PERTH results

### 506 3.2.1. Data correction procedure and tracer retrieval issues.

507 The previously described irrigation system issues resulted in a higher than desired variability of  
508 the imposed irrigation intensities, which led to an imperfect imposition of PSS conditions. A  
509 simple correction procedure was undertaken to circumvent this issue, in that the injection  
510 concentration was multiplied by  $x$ , where  $x$  is the ratio between the average irrigation intensity of  
511 each tracer injection divided by the average PSS irrigation intensity. This correction was  
512 performed to match the actual tracer input mass and the tracer input mass in "true" PSS.

513 We have also encountered data quality issues with the measured tracer quantities during the last 2  
514 cycles (not shown in **Figure 3C**) and decided to analyze the data only up to that moment. This led  
515 to a total of 10 days of experiment for the proceeding PERTH-based analysis, resulting in the  
516 ability to observe ages of water up to 10 days.

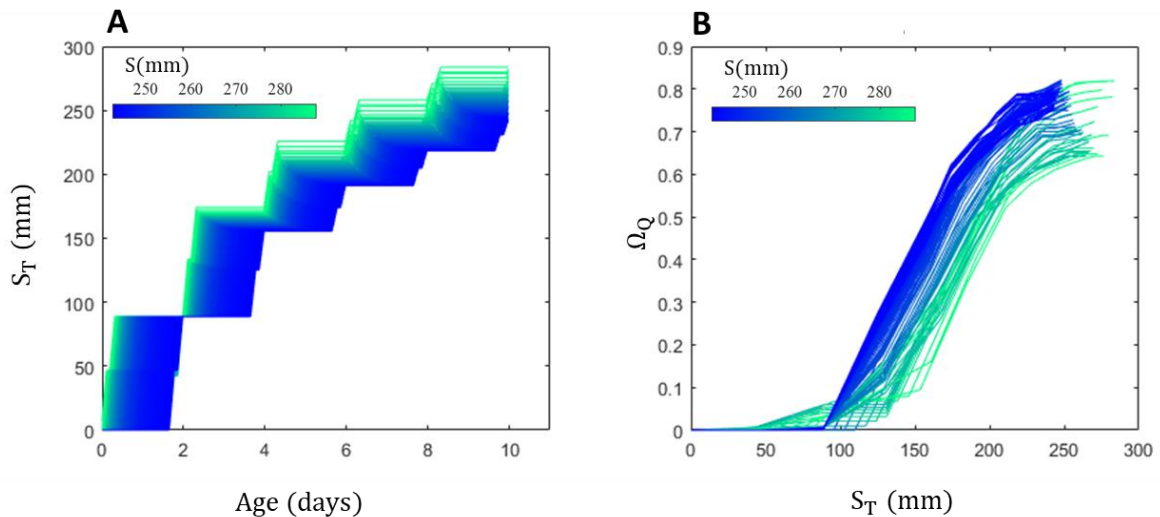
### 517 3.2.2. PERTH-Based Estimates of $S_T$ and $\Omega_Q$

518 The SAS components estimated through the PERTH methodology are presented in **Figure 5**.  
519 **Figure 5A** displays the values of  $S_T$  at each moment within the imposed 48-hour cycle, where  
520 colors from dark blue to light green denote low to high storage values, respectively. The observed  
521 convex shape of the  $S_T$  vectors throughout all storage levels denote a larger portion of younger  
522 water in comparison with older water in storage.

523 **Figure 5B** shows the retrieved  $\Omega_Q$  values following the same storage-assigned color scheme. The  
524  $\Omega_Q$  curves do not reach to 1, indicating imperfect mass recovery (Kim et al., 2016). Most  
525 importantly, it is possible to verify a general tendency of decreasing storage (light green towards  
526 dark blue) to be associated with a lateral shift in the  $\Omega_Q$  curves towards the left. This shift suggests  
527 that as storage decreases, more water having lower age-ranked storage is being sampled from the  
528 domain to leave the system. Conversely, higher storage values are associated with the selection of  
529 older water. This behavior has been commonly termed as direct storage effect (DSE), which is the  
530 opposite of the ISE, mentioned earlier. While the ISE seems to dominate at the catchment-scale

531 (Pangle et al., 2017; Benettin et al., 2017; Wilusz et al., 2017; Rodriguez et al., 2018; Kuppel et  
 532 al., 2020), the DSE has been less reported, and particularly associated with specific catchment  
 533 processes such as overland flow (Wilusz et al., 2020) while also being observed at the large-scale  
 534 LEO artificial hillslopes (Kim et al., 2021). While it is tempting to hypothesize what caused the  
 535 observed DSE based on the PERTH data alone, a more thorough discussion including the ERI  
 536 portion of the analysis is promoted further in the text.

537



538 **Figure 5. SAS components obtained by the application of the PERTH method over the 48-hour cycle. A –Age**  
 539 **ranked storage,  $S_T$ , with colors denoting total storage (mm). B – Storage selection functions ( $\Omega_Q$ ) at the**  
 540 **discharge, showing the shift towards the selection of waters having lower  $S_T$  with decreasing storage.**  
 541

542

### 543 3.3. Results from the ERI-PSS Method

544 The ERI-based observation of chloride movement within the lysimeter is discussed here. In section  
 545 **3.3.1** we discuss how bulk soil conductivity varied within the period prior to the tracer injection  
 546 (warmup period, i.e., the period where the system was in PSS though irrigation water kept at  
 547 background concentration), since this is an important aspect precluding the application of the PSS-  
 548 ERI method for obtaining values of fluid conductivity, as discussed in **2.4.2**. We then move on to  
 549 the discussion on the lysimeter-scale (as interpolated images along the y-z plane) chloride  
 550 breakthrough in section **3.3.2**. Information on the validation of the  $C_{Cl}$  estimates versus in-situ  
 551 observations as well as cross-sectional breakthrough images are shown as supporting information  
 552 (**Text S2, Figures S2 and S3, Table S1**).

553

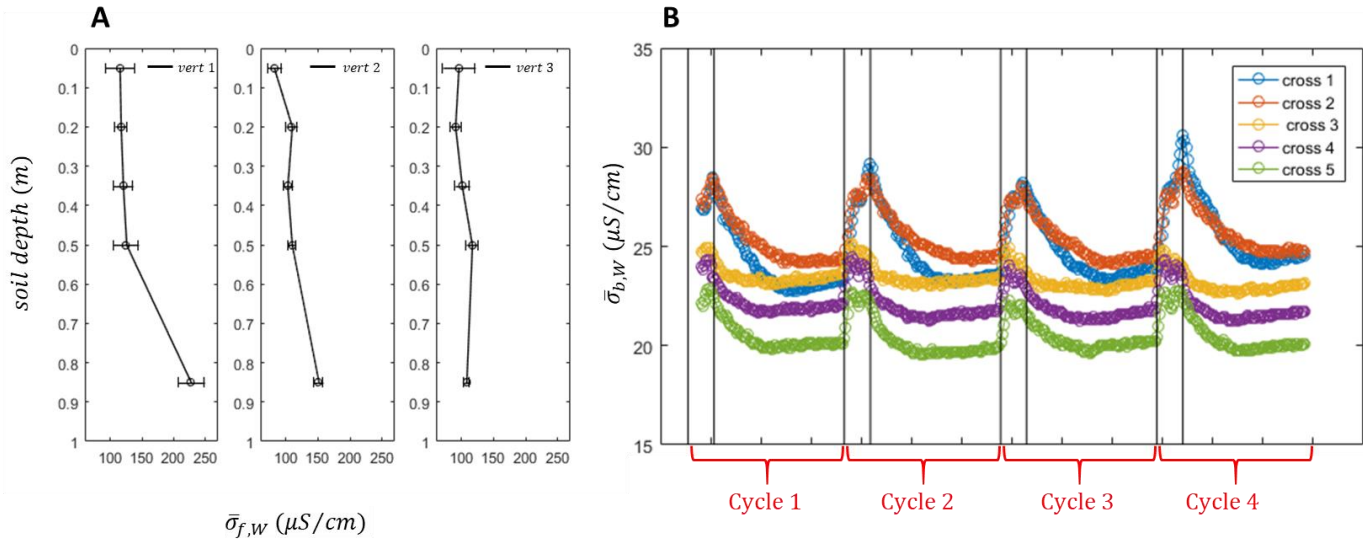
554 **3.3.1. Warmup Analysis**

555 **Figure 6A** shows the average warmup soil-water conductivity ( $\bar{\sigma}_{f,W}$ ) per sampling location for  
556 the 3 sampling verticals over cycles 1 through 6. Horizontal bars depict the temporal variability  
557 (as one standard deviation) observed throughout the warmup cycles. A gradient of increasing  
558 values  $\bar{\sigma}_{f,W}$  with soil depth is suggested as a function of distance from the outlet. The pattern of  
559 pre-injection fluid conductivities can be attributed to the release of solutes from the basaltic  
560 material into solution occurring as the result of geochemical weathering. An analysis performed  
561 by Pohlman et al., (2016) on the hydro-geochemical behavior of the LEO hillslopes showed that  
562 the regions further from the outlet experience enhanced rates of weathering due to longer rock-  
563 water contact times and lower fluxes.

564

565 During the warmup period the ERI-acquisition-system faced 2 stoppages, making it impossible to  
566 fully observe the cycles 5, 6 and 7. For this reason, we used cycles 1 through 4 for estimation of  
567 the pre-injection bulk conductivity values  $\sigma_{b,W}$ . For the purpose of visualization, **Figure 6B** shows  
568 cross-sectional averages of bulk conductivity for those cycles. The repeatability achieved  
569 throughout the experiment can be seen as the spike in  $\sigma_b$  values due to the irrigation pulses  
570 (represented by the vertical lines), followed by a falling limb, associated with the decrease in soil  
571 moisture. It can also be seen that average values increase from the cross-section closest to the  
572 outlet (C5) to the cross-section located upslope (C1). This behavior can be attributed to a  
573 combination of average moisture contents per cross-section and the observed increase in values  
574  $\sigma_f$  between the outlet and the upper boundary of the lysimeter, as seen in **Figure 6A**.

575



576 **Figure 6. Patterns of bulk soil conductivity and fluid conductivity during warmup. A-** Average  $\sigma_f$  obtained for  
 577 **the 3 water sampling verticals from the suction cups for the warmup period. Horizontal bars represent the**  
 578 **standard deviation of all measurements taken. The observed low variability in  $\sigma_f$  per sampling led to the choice**  
 579 **of constant (average) values in solving for  $\sigma_f$  after injection. B-ERI measurements: cross-sectional averages of**  
 580  **$\sigma_b$  for cycles 1 through 4, used to estimate the pre-injection response. The  $\sigma_b$  trajectories over time illustrate**  
 581 **the repeatability of the electrical conductivity as a response to a periodic oscillation of the internal variables.**  
 582 **Vertical bars represent beginning and end of irrigation pulses for each cycle.**

583

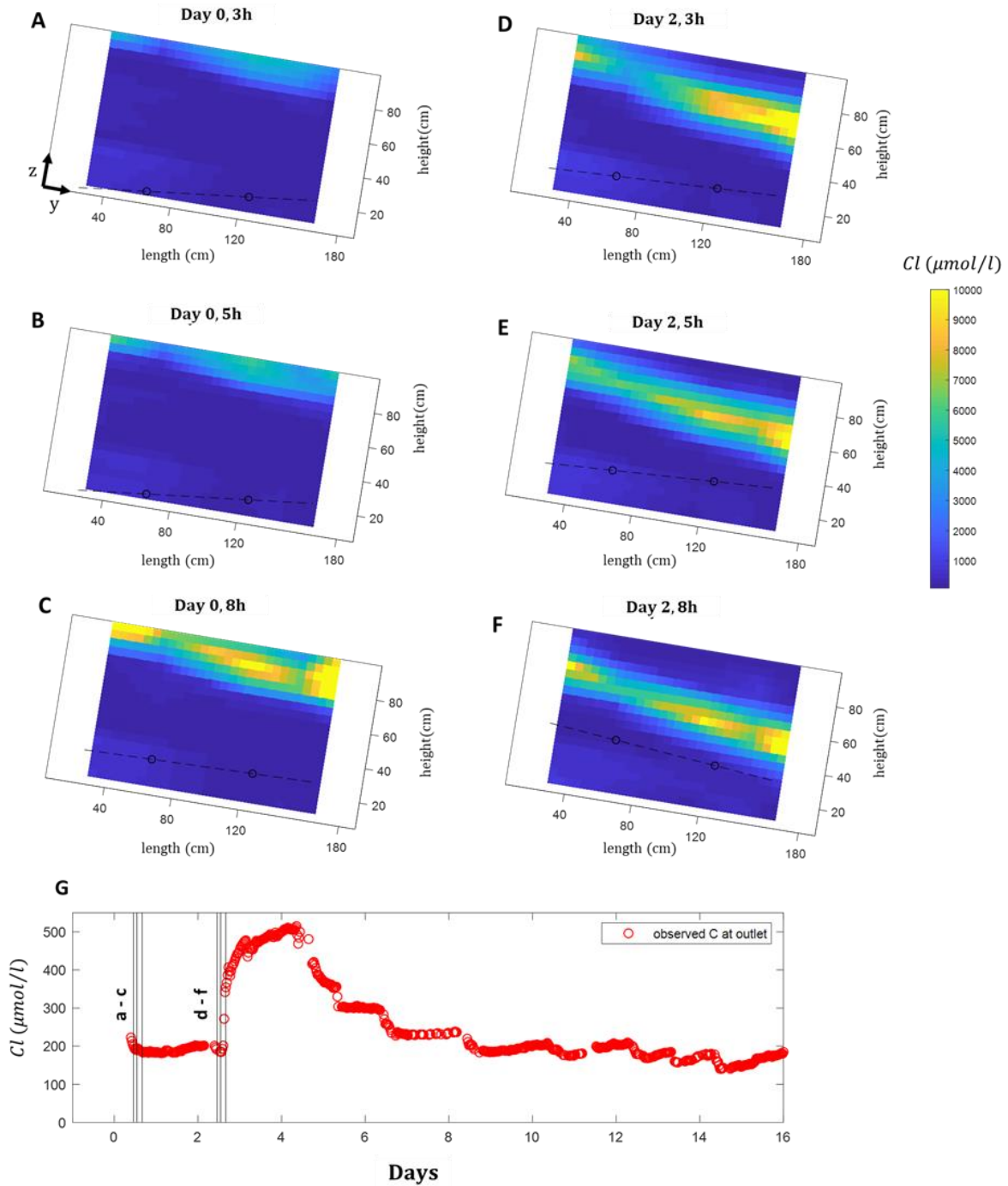
### 584 3.3.2. Lysimeter-Scale chloride Breakthrough

585 Here, we attempt to reconcile the 2D images of spatially interpolated chloride concentration with  
 586 the knowledge of the water table fluctuations (as discussed in 3.1) to further investigate the  
 587 lysimeter-scale chloride breakthrough, and explain the delayed response in discharge  
 588 concentration after the first recovery-period irrigation cycle (cycle 9, day 2), as seen in **Figure 3C**.  
 589 We should note that the final 2D sequence of Cl movement was subject to a manual procedure for  
 590 the correction of obvious artifacts. This was necessary due to the imperfections in the application  
 591 of PSS conditions, and possibly the influence of the assumptions on background fluid conductivity.  
 592 The corrections included removal of subtle oscillations in conductivity located further from the  
 593 tracer dominated area, substitution of negative conductivity values by 0, and truncation of  
 594 concentration values to avoid values higher than injection levels.

595 **Figure 7** provides an overlook of both ERI-derived solute movement and water table position at  
596 different times for the injection cycle (day 0) and first recovery cycle (day 2). The time stamps  
597 shown here were chosen to best represent the temporal dynamics described previously (see **Figure**  
598 **4**), in which  $t = 3\text{h}$  represents the first peak in water table at the end of the first irrigation pulse,  $t$   
599  $= 5\text{h}$  represents an intermediate water table height following a quick 2-hour recession prior to the  
600 second pulse, whereas  $t = 8\text{h}$  represents the water table at its highest level, immediately after the  
601 second irrigation pulse. Additionally, **Figure 7G** shows the progression of the chloride  
602 concentrations measured at the seepage face, with the timesteps of snapshots shown as vertical  
603 bars.

604 It can be seen that the tracer occupied a well-defined region within the first 25 cm of soil after the  
605 second irrigation pulse in day 0 (**Figure 7C**). It is possible to see that no tracer response has been  
606 detected at the seepage face for that day whereas the highest water table levels reached for that day  
607 were located somewhat far from the tracer-dominated region. On the other hand, on day 2 the  
608 tracer plume is pushed down further by the imposed irrigation pulses, allowing for a higher  
609 proximity between tracer dominated region and water table, which ultimately lead to the  
610 mobilization of the tracer. According to **Figure 7F**, most of the injected solute was placed above  
611 the water table at Day2, 8 hr. However, the solute concentration of discharge at that time is already  
612 high, which suggests the occurrence of lateral (along the y-direction) flow above the water table  
613 in the tension-saturated zone as the main process responsible for the quick tracer mobilization. The  
614 absence of an ERI cross-section closest to the seepage makes it impossible to accurately describe  
615 the chloride concentrations around that area, but the overall shape of the tracer plume suggests  
616 even deeper depths were reached within that region. It is also important to observe the differences  
617 between water table heights between both days, in which malfunctioning of the irrigation system  
618 being most likely the cause for the lower values of irrigation for day 0, resulting in lower water  
619 table levels.

620 An animation showing the progression of both water table fluctuations and solute movement  
621 within the lysimeter is provided (**supporting information Movie#1**) to aid the interpretation of  
622 the results.



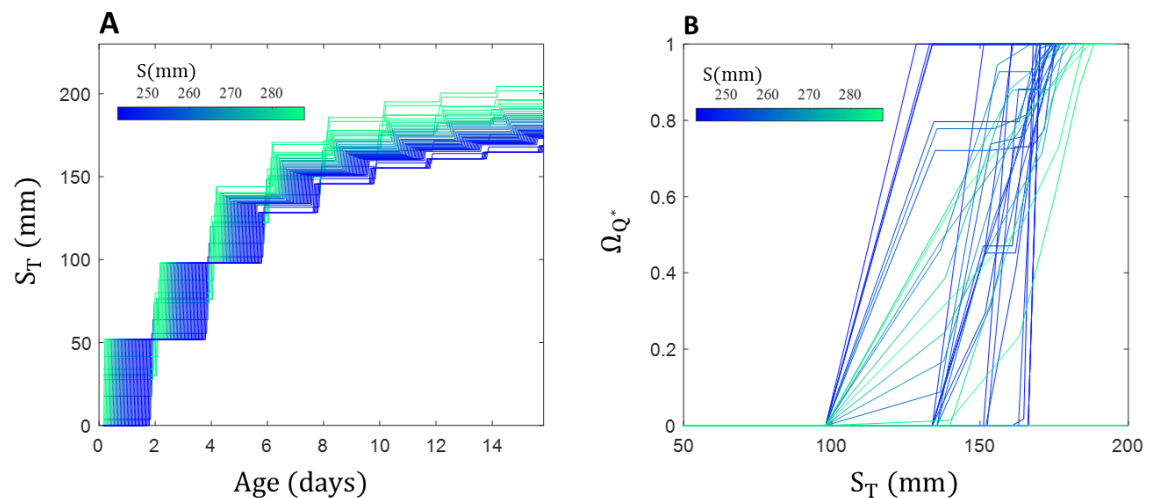
623

624 **Figure 7. (A-F) Interpolated ERT-derived panels showing chloride concentration in  $\mu\text{mol/l}$  throughout days 0**  
 625 **and 2 (tracer injection and following irrigation cycle). Dashed black lines indicate the approximate location of**  
 626 **the water table, estimated by pressure transducer measurements at 2 points (circles). G. Estimated chloride**  
 627 **concentration from discharge samples, highlighting the time-steps for which the panels A-F were taken.**

628

### 629 3.4. ERI-Based Estimates of $S_T$ and $\Omega_{Q^*}$

630 The SAS components obtained through the ERI-based chloride breakthrough are depicted in  
 631 **Figure 8**. The predominance of younger water is indicated by the overall convex pattern be  
 632 observed in **Figure 8A**. The difference in “surveyed” volumes by both methods can be seen when  
 633 comparing the highest magnitudes of  $S_T$  between **Figure 8A** and **Figure 5A**, which is likely due  
 634 to the fact that the ERI domain does not capture the whole lysimeter, leading to different storage  
 635 totals. The  $\Omega_{Q^*}$  functions estimated through ERI (**Figure 8B**) do not display the same smoothness  
 636 as in the PERTH-based estimation of  $\Omega_{Q^*}$ , where the shift towards selection of lower values of  $S_T$   
 637 with decreasing storage values is not as readily observed. Moreover, it can be seen in **Figure 8B**  
 638 that some curves at the lower storage (dark blue colors) exhibited constant values within certain  
 639 intervals of  $S_T$ . Such pattern can be understood as an indication that certain ranges of  $S_T$  were not  
 640 sampled for those time-steps. Additionally, the ERI-based  $\Omega_{Q^*}$  seen in **Figure 8B** reach the value  
 641 of 1. This can be explained by the fact that the changes in age rank storage density estimated within  
 642 the ERT domain were normalized by the change in storage within the domain ( $Q^*$ ).



643  
 644 **Figure 8-** SAS components derived from the pixel-based analysis of ERI images. **A** – Storage selection functions ( $\Omega_Q$ )  
 645 at the discharge, showing the shift towards the selection of waters having lower  $S_T$  with decreasing storage.  
 646  
 647

### 648 3.5. Reconciling the Time-Varying SAS Functions and Spatial Distribution of Ages.

649 Here, we attempt to shed light at the physical mechanisms giving rise to the observed temporal  
650 patterns of age-ranked storage and storage selection functions (**Figure 5** and **Figure 8**) throughout  
651 the representative cycle. To do so, we extend our analysis to include ERI-based images of water  
652 ages and the associated progression of the backwards transit time distribution (bTTD), while also  
653 considering the total storage and water table fluctuations.

654 **Figure 9A** summarizes the lysimeter's storage ( $S$ ) and irrigation flux ( $I$ ) at four distinct moments.  
655 The timestamps of 3, 8, 16 and 40 hours were taken to represent the progression of storage caused  
656 by the irrigation pulses and discharge out of the lysimeter, as discussed in **3.1** and **Figure 4**. Storage  
657 reaches a first peak at 3h as a result of the first irrigation pulse, and is followed by a second, higher  
658 peak, at the end of the second irrigation pulse, at 8h. Storage recession starts then, where the 16-  
659 and 40-hour labels represent early and late recession moments.

660 The spatial distribution of water ages within the lysimeter for the 4 different moments are  
661 highlighted in **Figure 9B, D, F and H**. These images display the most frequent age value found  
662 in each pixel,  $\mathcal{T}^*$ , with yellow representing older water and dark blue representing younger water.  
663 To facilitate the visualization of where each age was most likely to be found throughout the  
664 progression of the experiment, we highlighted, in red, the values of water ages at the injection  
665 moment for the 3-hour snapshot **Figure 9B** (the actual ages at that moment should be incremented  
666 by 3 hours).

667 Also shown are the approximate water table locations, which will be discussed further in this  
668 section. The observation of  $\mathcal{T}^*$  values on the left-side images makes some observations possible.  
669 A distinctive pattern is clear between all time-steps, in which water with older ages are found at  
670 the bottom left region of the lysimeter with mean age values decreasing both towards the lysimeters  
671 outlet as well as towards the soil surface. Both vertical and lengthwise patterns were somewhat  
672 expected from the chloride breakthrough observed in **Figure 7**: regions that have "seen" the  
673 chloride tracer comparatively later than others and where the tracer stayed for longer are assigned  
674 higher values of  $\mathcal{T}^*$ . In other words, longer residence times suggested by the chloride tracer  
675 progression were translated into higher values of  $\mathcal{T}^*$ , whereas more *active* regions are associated  
676 with lower  $\mathcal{T}^*$  values. It is also possible to notice the effect of the irrigation water being added to  
677 the lysimeter as the increase in the extent of the region having low  $\mathcal{T}^*$ , extending vertically  
678 downwards from the soil surface (**Figure 9B and D**, 3 and 8 hours respectively). Additionally, the

679 spatial distribution of  $\mathcal{T}^*$  at the later time-step (**Figure 9H**, 40 hours) shows a very similar pattern  
680 to the one at 16 hours (**Figure 9F**), the latter having overall lighter hues. This similarity indicates  
681 that the depth reached by the water applied with the rainfall did not change noticeably over the  
682 drying period, while the effect of ageing of water can be seen in the dimming of the colors.

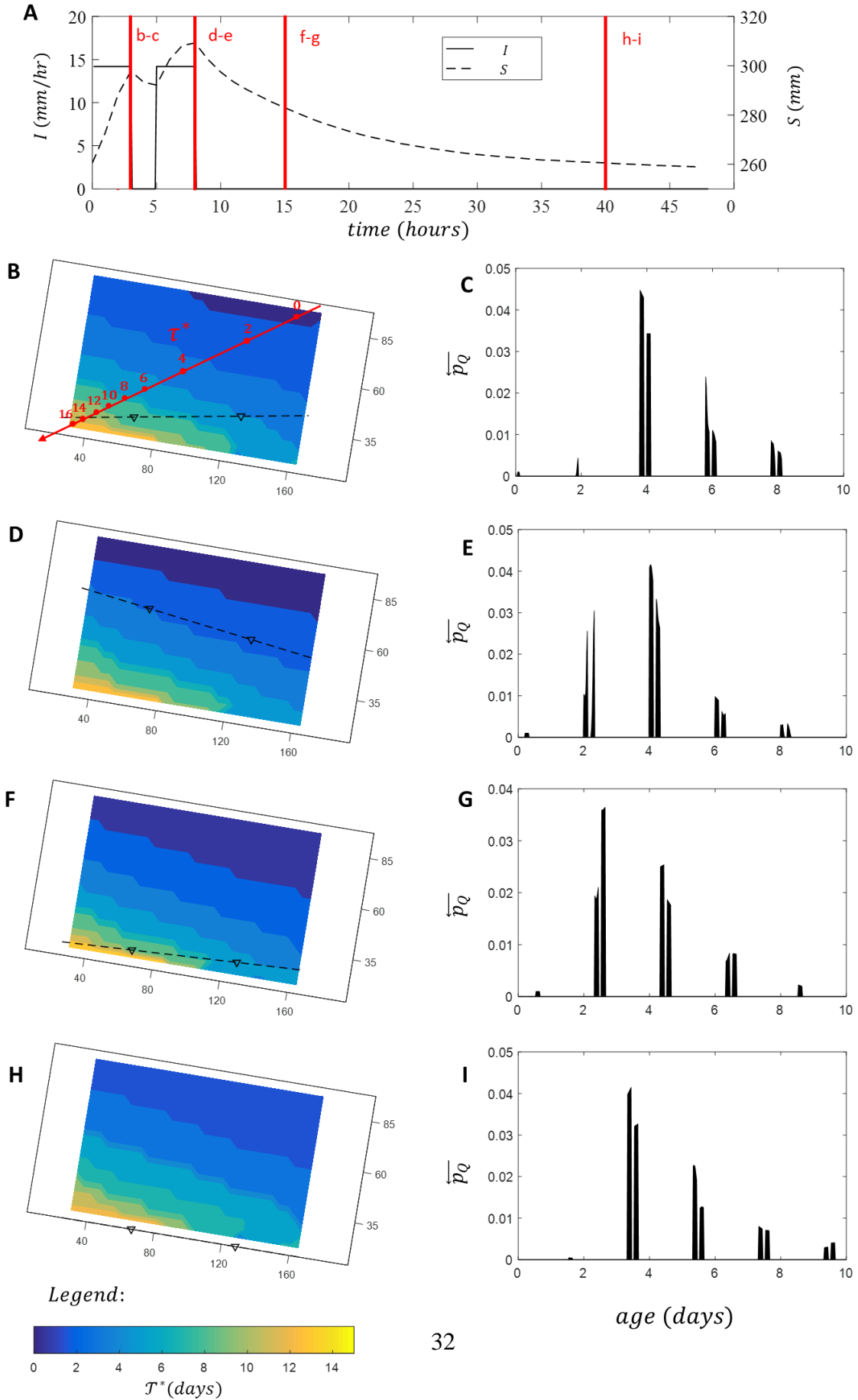
683 We then calculated the backwards transit time distribution in its *density* form ( $\tilde{p}_Q$ ) for the same  
684 snapshots for a combined analysis of the ages of water being discharged through time. These  
685 results can be seen on the right-side, as **Figure 9C, E, G and I**. It is possible to see that the end of  
686 the first rain pulse (**Figure 9C**) marks the moment where 2-day old water starts becoming present  
687 in the discharge, although in a very small amount. At the end of the second pulse, when the storage  
688 (and discharge) is at its highest, we see a greater portion of 2 days-old water being selected (**Figure**  
689 **9E**). Following that, as the lysimeter starts experiencing ever decreasing storage values, the  
690 proportion of 2 days-old water being discharged is then increased in the subsequent moments  
691 (**Figure 9E through I**).

692 Note that as time progresses, water once labeled as 2 days old (as seen at the beginning of the  
693 cycle) will reach the age of 4 days at the end of the cycle. In this way, at 40 hours, the youngest  
694 water being discharged is now closer to being 4 days old, and the overall shape of the  $\tilde{p}_Q$   
695 distribution now resembles the configuration seen at the beginning of the cycle (**Figure 9I**).  
696 Although less abundant, older water having ages between 6 and 10 days old also appear in the  
697 discharge.

698 The analysis of both water table levels, and internal age distribution can then be used to suggest  
699 the mechanisms behind the observed progression of  $\tilde{p}_Q$ : **Figure 9H and I** can be taken as a  
700 snapshot of the initial conditions prior to the first pulse. Prior to the first irrigation pulse, the initial  
701 (low) levels of storage lead to the saturation occurring only at a small region around the seepage  
702 face (although not detected by the 2 pressure transducers, but necessary to exist in order for  
703 discharge to occur) in which water predominantly with ages 4 days and older are present. Although  
704 the seepage face region lies outside of the ERI domain, such pattern in older ages is strongly  
705 suggested by visual inspection of the color bands at the lower right corner of the surveyed region  
706 in **Figure 9H**. Following that, the imposed irrigation causes the water table to rise (**Figure 9B**)  
707 increasing the saturated area around the seepage face, which however still discharges water from  
708 the same pool of ages. The irrigation water (age = 0 days) however displaces the water near the

709 surface (age = 2 days) downwards. The subsequent irrigation pulse displaces the 2-day-old water  
710 further downwards, while also increasing water table levels (**Figure 9D**). This combined effect of  
711 downwards movement of 2-day-old water and rising water table levels brings the 2-day-old water  
712 closer the saturated region (note the water table line intersects the region of ages  $\approx 2$  days) where  
713 it begins to be mobilized (**Figure 9B, C, D and E**). The 2-day-old water is then further mobilized  
714 during the recession of the water table (**Figure 9F and G**), suggesting a continuing interaction  
715 between the 2-day-old saturated region closer to the seepage face. At the end of the cycle, the once  
716 2-day-old region of the domain is now close to being 4-days old. This can be further verified as  
717 the distribution of ages in **Figure 9I** can be seen as resulting from a lateral shift applied to the ages  
718 in **Figure 9G**. The system is then subject to another cycle, in which the processes described above  
719 take place once again. It is also important to note the role the saturated zone likely plays in releasing  
720 older water. Due to the distance between the 10 days-old region and the seepage face, the preceding  
721 analysis cannot explain the exact timing when such waters will be seen at the seepage face, since  
722 its saturation will not be translated into a quick release, as it might have happened with the seepage  
723 face region. However, the increase in the extent of the saturated area towards the back of the  
724 lysimeter might help its mobilization at later periods.

725 To facilitate the interpretation, an animation showing the above results is provided as a  
726 supplemental material (**supporting information, Movie #2**).



728

729 **Figure 9. Evolution of water ages within the lysimeter in comparison with backward-transit-time distributions**  
 730 **for 4 distinct moments within the representative cycle. Subplot A shows the moments being depicted in terms**  
 731 **of the total storage within the system. Subplots B, D, F and H display the most frequent water age  $\tau^*$  per pixel.**  
 732 **Dashed lines represent the estimated location of the water table throughout the chosen moments. Subplots C,**  
 733 **E, G and I display the backwards transit time distribution ( $\overline{p}_Q$ ) observed at each of the selected moments. Insets**  
 734 **are shown to highlight smaller values  $\overline{p}_Q$ , associated with older ages (10-14 days-old).**

735

## 736 **4. Discussion**

### 737 **4.1. Observed Mechanisms Shaping Age Selection.**

738 Our results highlight the interplay between the downward infiltration and the upward saturation  
 739 resulting in a “layering” of water ages with depth, along with the selection of water ages for  
 740 discharge being controlled by the spatial and temporal changes in flowpath direction imposed by  
 741 a dynamic water table. Even though the wetting of the lysimeter led to an extension of the saturated  
 742 area contributing to discharge, such areas were occupied by pre-event water throughout the whole  
 743 experiment. We have observed a somewhat constant contribution of pre-event water for most of  
 744 the wetting period, while fractions of younger water started interacting with the saturated region,  
 745 and being released, when the lysimeter reached a high storage level. After that, younger water  
 746 fractions continued being released in an increasing fashion as the water table receded. Even though  
 747 our surveyed region did not allow for its direct observation, the most likely reason for the  
 748 continuing release of the younger water with a decreasing water table was the existence of a  
 749 permanent saturated region closer to the seepage face which might have being reached by the  
 750 downwards-displaced younger water fraction, allowing for its mobilization.

751 As mentioned in **3.2.2**, many studies performed at the catchment scale point out to the behavior in  
 752 which increasing storage is associated with the discharge of younger water (Harman, 2015;  
 753 Benettin et al., 2017; Wilusz et al., 2017; Kuppel et al., 2020). Fewer investigations have reported  
 754 the DSE. For example, Wilusz et al., (2020) has shown direct storage effect to be widespread  
 755 within individual flowpaths, while the catchment as a whole behaves according to an ISE. The  
 756 authors attribute the seemingly paradoxical finding to the disproportional release of younger water,  
 757 mainly from overland flow during storms. Similarly, in a recent study performed at the 3 large-  
 758 scale, LEO artificial hillslopes, Kim et al., (2020) applied the PERTH method and also found the  
 759 direct storage effect to occur. We think our study can be seen as an example of how a specific

760 catchment unit (in this case a hillslope, or the section of the hillslope closer to the stream, with an  
761 impermeable lower boundary) might behave following a DSE.

#### 762 **4.2. Comparison with Previous PERTH Experiment and its Implications**

763 Additional insights about the mechanisms controlling the time-variable SAS components can be  
764 gained by comparing the results presented here with other studies applying the PERTH method  
765 applied at the same lysimeter (Kim et al., 2016; Pangle et al., 2017). Although the same lysimeter  
766 has been used, we should note that it has been destructively sampled (Sengupta et al., 2016) and  
767 further repacked between experiments. Most importantly the same basaltic soil was added  
768 following the same packing procedure prior to our experiment. Also, the rainfall patterns imposed  
769 by the irrigation system did suffer from a slight modification leading to higher rainfall intensities  
770 experienced at the lower end of the lysimeter.

771 Kim et al. (2016) found the system to be characterized by an inverse storage effect. The explanation  
772 for the ISE was only broadly hypothesized in the latter study, and further explored through a 2D  
773 numerical modeling of solute transport and hydrologic fluxes shown in Pangle et al., (2016). Both  
774 studies suggest a rapid mobilization of younger water promoted by the rising water table as the  
775 mechanism resulting in the inverse-storage effect.

776 We believe the characteristics of the hydrologic regime to be one of the main reasons why a  
777 different storage effect has been observed. For the experiment of Kim et al., (2016) the PSS cycle  
778 consisted of a more intense hydrologic forcing: a 24-hour cycle was imposed, whereas two 4.5  
779 hour-long irrigation pulses were applied with an interval of 7.5 hours in between: the first pulse  
780 had a low intensity period (13 mm/hr for 1.5 hour) followed by a high intensity one (26 mm/hr for  
781 the remaining 1.5 hour), and the second pulse had a high intensity followed by a low intensity,  
782 both having the same duration as in the first pulse. When comparing to the 48-hour cycle applied  
783 in this study, a difference of 72 mm in total volume of water added per cycle can be estimated (156  
784 mm versus 84 mm), representing an 86% increase in total irrigation volume, being applied in half  
785 of the time. This resulted in a contrasting internal functioning, where a permanent water table  
786 (measured at the same locations as in this study) of approximately 40 cm was present during dry  
787 (low storage) states, which is close to the maximum water table level measured in this study (55  
788 cm). On the other hand, the highest water table seen in Kim et al., (2016) reached levels up to 80  
789 cm during wet periods (high storage). The longer drying periods and an almost complete extinction

790 of the water table between events, together with lower water table levels at wetter conditions  
791 precluded the release of event water in our experiment, and also contributed to the delayed  
792 discharge of younger water, which occurred predominantly during the recession of the water table,  
793 thus characterizing the DSE as suggested by the movement of the  $\Omega_Q$  function (**Figure 5B**).

794 The fact that different storage effects can occur through the same basic mechanisms (downward  
795 infiltration and water age selection by a dynamic water table), might serve as an evidence on the  
796 role of external variability imposed by climate in shaping the SAS functions and the resulting  
797 storage effects. Indeed, the results from this experiment align with the commonly held hypothesis  
798 of drier systems releasing predominantly older water (Botter et al., 2010; Heidbuchel et al., 2013;  
799 Wilusz et al., 2017). We believe the cycle imposed at the lysimeter in this study to be an example  
800 of a “drier” regime, whereas the previous experiment (Kim et al., 2016) an example of a “wetter”  
801 regime.

802 Aside from the characteristics of the imposed irrigation cycles, soil structure might also have an  
803 important role in explaining the differences in both experiments. Pangle et al., (2016) were only  
804 able to reproduce the ISE in their numerical experiment after the inclusion of substantial soil  
805 heterogeneity, in which the hydraulic conductivities were assumed to decrease with both depth  
806 (along the z-dimension, decreasing from the soil surface downwards), as well as length (along the  
807 y-dimension, decreasing towards the seepage face). Such soil heterogeneity was assumed to be  
808 caused by soil compaction and was corroborated by actual measurements of bulk density from  
809 within the lysimeter (Sengupta et al., 2016). Low hydraulic conductivity values at the bottom-right  
810 side of the lysimeter might have contributed to the occurrence of faster flow-paths closer the  
811 surface, which would facilitate the export of younger waters as seen in the studies from Kim et al.,  
812 (2016) and Pangle et al., (2016). The soil used in our experiment was present in the lysimeter for  
813 less time and experienced less irrigation cycles. We believe this could have led to less soil  
814 compaction, leading to a different soil structure from the one previously reported. The discussion  
815 of how different the spatial distribution of soil properties was in our experiment in comparison to  
816 the previous PERTH experiment is, however, beyond the scope of this paper and would benefit  
817 from numerical experiments as well as the measurement of hydraulic properties, as it has been  
818 done previously.

819

### 820 **4.3. Limitations and Suggestions for Future Applications**

821 Our findings on the mechanisms ultimately shaping the SAS functions behavior will naturally be  
822 subject to the limitations of a controlled, laboratory study. The rainfall regime imposed to the  
823 lysimeter was not chosen to represent a specific climate, and the LEO basaltic soil was  
824 “engineered” to facilitate the detection of incipient pedogenesis (Pangle et al., 2015). Also, the flat  
825 impermeable boundary of the soil lysimeter might not represent commonly observed bedrock  
826 features (Gabrielli et al., 2012). Our study can nonetheless stir the discussion on how ages of water  
827 observed in the discharge are dynamically linked to internal processes that are universal to many  
828 watersheds, as it has provided observational evidence of how both infiltration and saturation from  
829 the bottom might interact and determine time-varying SAS functions. As the study of water ages  
830 has been many times pursued in saturated versus unsaturated hydrologic compartments (Sprengrer  
831 et al., 2019), our experiment was able to explore age dynamics in which both spatial and time-  
832 varying degrees of saturation occurred.

833 Some limitations imposed by the ERI procedure used here are also worth discussing. The most  
834 important one being that a full-lysimeter picture of the ERI-derived ages of water would be  
835 preferred. The extension of the survey to include the whole lysimeter would allow for a better  
836 assessment of the lysimeter-scale chloride breakthrough, and a direct comparison between ERI-  
837 and PERTH-based results. Due to the strong boundary effects, especially around the seepage face  
838 (see how the age-labelled bands tend to “sink” faster closer to the seepage face, in **Figure 9** and  
839 **Figure S2**), we believe that actually measured resistivity/conductivity values around the  
840 extrapolated regions to be preferred when extending the ERI results into the PERTH analysis.  
841 Also, the choice for the acquisition of 2D cross-sectional panels was motivated not only by the  
842 constraints imposed by the lysimeter structure onto the location of the electrodes (see Methods  
843 Section), but also by time constraints. As mentioned previously, 35 minutes were necessary, on  
844 average, for a full scan over the 5 cross-sections. The choice of a 3D survey would invariably  
845 increase the survey time, leading to poor temporal coverage of the processes. An ERI system with  
846 more channels than what was used here (SuperSting® R8, 8 channels) could allow for a faster  
847 image acquisition and therefore the possibility of 3D surveys.

848 The precision with which the PSS was applied also posed additional challenges for an adequate  
849 ERI-based value of Cl concentration. The PSS assumption is of fundamental importance for the  
850 estimation of actual  $\sigma_f$  as seen in the normalization procedure shown in **Equation 14**. Equally

851 important is the estimation of background (pre-injection) fluid conductivity values in the same  
852 equation. Our spatial estimates were taken by spatial interpolation and extrapolation of observed  
853 values at sampling locations (see **Figure 1**). This might have resulted in poor estimation at regions  
854 further from the suction cups. While we have attempted to correct clear artifacts in the final images  
855 of Cl concentration, through the semi-manual cleaning/filtering procedure described in **3.3.2**, it is  
856 not clear whether such procedure was entirely successful to correct for the aforementioned issues.

857 We believe there is great potential in extending the PERTH method for ERI applications, and that  
858 should include applying it at different settings. The procedure as shown here could be tested in  
859 other controlled facilities, such as monitored lysimeters, and hillslope transects. The large-scale  
860 LEO artificial hillslopes are equipped with ERI capabilities, and the application of the PERTH-  
861 ERI method might provide valuable insight into their internal functioning, thus aiding the  
862 understanding of water age dynamics at the hillslope scale.

863 We also envision the application of our method in the field, in which the ERI procedure alone can  
864 be followed without the need for validation based on output-based tracer concentration. As  
865 provided in the supporting information, a modified procedure should be followed to allow the  
866 application of the method on soils with significant surface conduction (mainly soils with clay  
867 minerals). Localized sprinkling experiments can provide the necessary PSS conditions at smaller  
868 regions to study for example infiltration under different land cover types and the resulting age  
869 distribution.

## 870 **5. SUMMARY**

871 This study presents the results of an experiment to analyze the time-variable TTD in which an  
872 output-based tracer sampling allowed for a lumped-system approach and an ERI-based method  
873 was used for the estimation of water ages internally. Our system was a 1m<sup>3</sup> sloping soil lysimeter,  
874 which allowed for the observation of some hydrologic processes seen at natural hillslopes.

875 We used the PERTH (Harman and Kim, 2017) method to provide estimates of TTD, which  
876 returned in the progression in the ages of water being selected to leave the system as discharge.  
877 The PERTH method relies on a rainfall scheme in which a representative hydrologic cycle is  
878 repeated several times with tracers being added throughout the experiment and retrieves the  
879 progression of TTD within a representative cycle following the SAS framework. We have also  
880 introduced the use of ERI as a tool for the investigation of the processes leading to the varying

881 residence times of water. We demonstrated that the PSS theory (Harman and Kim, 2014) can be  
882 applied to the equations governing the electrical conductivity of soils to provide a simple solution  
883 to the tracer movement under complex conditions. Our method is advantageous over the existing  
884 approaches in that it does not require knowledge of petrophysical properties of the material for  
885 estimating fluid conductivities that can be applied at transient conditions. The ERI-based method  
886 yields additional insights on the time-variability of water ages within the representative cycle and  
887 also be used to estimate lumped parameters from the SAS framework.

888 The results from the combination of both methods promoted a discussion on the internal  
889 mechanisms taking place as TTD evolve through time as a function of system storage: As the  
890 system experienced two subsequent irrigation pulses, it transitioned from dry (low storage)  
891 towards wet (high storage) conditions, followed by a transition from wet to dry (high-to-low  
892 storage) as the irrigation stopped. At the first pulse leading to a “wetting” stage the system  
893 discharged predominantly older water, whereas as fractions of younger water started being  
894 released when the system achieved its highest storage and increased as the system underwent a  
895 “drying” stage. This mechanism can be explained by the downwards movement of the younger  
896 water being pushed by the applied irrigation alongside with the development of a water table. No  
897 event water (i.e. event water being added by the current irrigation pulse) was ever discharged,  
898 since the water table did not rise high enough to reach the region with the youngest water. On the  
899 other hand, water from the preceding event was released when the region containing waters with  
900 that age became saturated, allowing for its quicker mobilization. Since the mobilization started at  
901 the moment of highest storage and proceeded with the drying of the system, the system was  
902 characterized for the most part as having a direct storage effect.

903 Our results suggest that the internal assessment of ages to be valuable for unraveling the  
904 mechanisms leading to the time-variability of TTD. By comparing our results to a similar study  
905 performed at the same system, we were able to hypothesize the controls of climate, seen as the  
906 frequency of rainfall events, and the spatial distribution soil properties, as important controls on  
907 how ages of water of discharge might be selected from hydrologic systems.

908 Finally, although this study suffers from the inherent limitations of the system being used, i.e., an  
909 artificial hillslope transect, we were able to provide an in-depth analysis of the mechanisms driving  
910 water age dynamics that are present in specific watershed units. While the study of water ages is

911 traditionally performed through lumped systems approaches or physically based modelling, the  
912 opportunity to directly observe how water ages vary within and out of the domain of interest should  
913 be an exciting venue for the advancement of hydro chronology studies.

914 **ACKNOWLEDGEMENTS**

915

916 Antonio A. M. N. would like to acknowledge the financial support received by the Brazilian  
917 Ministry of Education through the CAPES Foundation and the State of Espírito Santo through  
918 the FAPES foundation. We would like to thank Ty Ferré (University of Arizona) and Andrew  
919 Binley (Lancaster University) on suggestions on electrode design and Michael Tso (Lancaster  
920 University) for the support with the program R3. Additionally, the authors would like to thank  
921 the Biosphere 2 staff involved in the operational aspects of the experiment: Aaron Bugaj, Nate  
922 Abramson, Wei-Ren Ng and Edward Hunt. Upon acceptance, the data used in this study will  
923 be available through: [https://figshare.com/authors/Antonio\\_Meira/8292240](https://figshare.com/authors/Antonio_Meira/8292240)

924

925 **REFERENCES**

926 Alumbaugh, D. L., Labrecque, D., Technologies, M., Yeh, T. C. J., De-fg-, G. N., Project, G., &  
927 Roland, O. (n.d.). US Department of Energy A HYDROLOGIC - GEOPHYSICAL  
928 METHOD FOR CHARACTERIZING FLOW AND TRANSPORT PROCESSES WITHIN  
929 THE VADOSE ZONE Project Number : 70267

930 Ameli, A. A., Amvrosiadi, N., Grabs, T., Laudon, H., Creed, I. F., McDonnell, J. J., & Bishop,  
931 K. (2016). Hillslope permeability architecture controls on subsurface transit time  
932 distribution and flow paths. *Journal of Hydrology*, 543, 17–30.  
933 <https://doi.org/10.1016/j.jhydrol.2016.04.071>

934 Archie, G. E. (1942), The electrical resistivity log as an aid in determining some reservoir  
935 characteristics, *Trans. Am. Inst. Min. Metall. Pet. Eng.*, 146, 54–62.

936 Bellmunt, F., Marcuello, A., Ledo, J., & Queralt, P. (2016). Capability of cross-hole electrical  
937 configurations for monitoring rapid plume migration experiments. *Journal of Applied*  
938 *Geophysics*, 124, 73–82. <https://doi.org/10.1016/j.jappgeo.2015.11.010>

939 Benettin, P., C. Soulsby, C. Birkel, D. Tetzlaff, G. Botter, and A. Rinaldo (2017), Using SAS  
940 functions and high-resolution isotope data to unravel travel time distributions in headwater  
941 catchments, *Water Resour. Res.*, 53, 1864–1878, doi:10.1002/2016WR020117

- 942 Binley, A. (2013), R3t, Version 1.8., Lancaster Univ., Lancaster, U. K. (Available at  
943 <http://www.es.lancs.ac.uk/people/amb/Freeware/Freeware.htm>.)
- 944 Binley, A., Henry-Poulter, S., & Shaw, B. (1996). Examination of solute transport in an  
945 undisturbed soil column using electrical resistance tomography. *Water Resources Research*,  
946 *32*(4), 763–769.
- 947 Binley, A., Hubbard, S. S., Huisman, J. A., Revil, A., Robinson, D. A., Singha, K., & Slater, L.  
948 D. (2015). The emergence of hydrogeophysics for improved understanding of subsurface  
949 processes over multiple scales. *Water Resources Research*, *51*, 3837–3866.  
950 <https://doi.org/10.1002/2015WR017016>.Received
- 951 Botter, G., Bertuzzo, E., & Rinaldo, A. (2010). Transport in the hydrologic response: Travel time  
952 distributions, soil moisture dynamics, and the old water paradox. *Water Resources*  
953 *Research*, *46*(3), 1–18. <https://doi.org/10.1029/2009WR008371>
- 954 Botter, G., Bertuzzo, E., & Rinaldo, A. (2011). Catchment residence and travel time  
955 distributions: The master equation. *Geophysical Research Letters*, *38*(11), 1–6.  
956 <https://doi.org/10.1029/2011GL047666>
- 957 Brantley, S. L., Goldhaber, M. B., & Vala Ragnarsdottir, K. (2007). Crossing disciplines and  
958 scales to understand the critical zone. *Elements*, *3*(5), 307–314.  
959 <https://doi.org/10.2113/gselements.3.5.307>
- 960 Campbell, R. B., Bower, C. A., & Richards, L. A. (1948). Change of Electrical Conductivity  
961 With Temperature and the Relation of Osmotic Pressure to Electrical Conductivity and Ion  
962 Concentration for Soil Extracts. *Soil Science Society of America Journal*, *13*(C), 66–69.  
963 <https://doi.org/10.2136/sssaj1949.036159950013000c0010x>
- 964 Cvetkovic, V. (2011). The tempered one-sided stable density: A universal model for  
965 hydrological transport? *Environmental Research Letters*, *6*(3). [https://doi.org/10.1088/1748-](https://doi.org/10.1088/1748-9326/6/3/034008)  
966 [9326/6/3/034008](https://doi.org/10.1088/1748-9326/6/3/034008)

- 967 Danesh-Yazdi, M., Klaus, J., Condon, L. E., & Maxwell, R. M. (2018). Bridging the gap  
968 between numerical solutions of travel time distributions and analytical storage selection  
969 functions. *Hydrological Processes*, 32(8), 1063–1076. <https://doi.org/10.1002/hyp.11481>
- 970 Dontsova, K., Steefel, C. I., Desilets, S., Thompson, a., & Chorover, J. (2009). Coupled  
971 modeling of hydrologic and geochemical fluxes for prediction of solid phase evolution in  
972 the Biosphere 2 hillslope experiment. *Hydrology and Earth System Sciences Discussions*, 6,  
973 4449–4483. <https://doi.org/10.5194/hessd-6-4449-2009>
- 974 Gabrielli, C. P., McDonnell, J. J., & Jarvis, W. T. (2012). The role of bedrock groundwater in  
975 rainfall-runoff response at hillslope and catchment scales. *Journal of Hydrology*, 450–451,  
976 117–133. <https://doi.org/10.1016/j.jhydrol.2012.05.023>
- 977 Geuzaine, C., Remacle, J. F. (2009). Gmsh: A 3-D finite element mesh generator with built-in  
978 pre- and post-processing facilities. *International Journal for Numerical Methods in*  
979 *Engineering*, 79(11), 1309–1331. <https://doi.org/10.1002/nme.2579>
- 980 Harman, C. J. (2015). Time-variable transit time distributions and transport: Theory and  
981 application to storage-dependent transport of chloride in a watershed. *Water Resources*  
982 *Research*, 51(1), 1–30. <https://doi.org/10.1002/2014WR015707>
- 983 Harman, C. J., and Kim, M. (2014), An efficient tracer test for time-variable transit time  
984 distributions in periodic hydrodynamic systems, *Geophys. Res. Lett.*, 41, 1567– 1575,  
985 doi:10.1002/2013GL058980.
- 986 Heidbüchel, I., Troch, P. a., & Lyon, S. W. (2013). Separating physical and meteorological  
987 controls of variable transit times in zero-order catchments. *Water Resources Research*, 49,  
988 7644–7657. <https://doi.org/10.1002/2012WR013149>
- 989 Jury, W. A. (1982). Simulation of solute transport using a transfer function model. *Water*  
990 *Resources Research*, 18(2), 363–368. <https://doi.org/10.1029/WR018i002p00363>
- 991 Kemna, A., Kulesa, B., & Vereecken, H. (2002). Imaging and characterisation of subsurface  
992 solute transport using electrical resistivity tomography (ERT) and equivalent transport

- 993 models. *Journal of Hydrology*, 267, 125–146. <https://doi.org/10.1016/S0022->  
994 1694(02)00145-2
- 995 Kim, M., Pangle, L. A., Cardoso, C., Lora, M., Volkmann, T. H. M., Wang, Y., ... Troch, P. A.  
996 (2016). Transit time distributions and StorAge Selection functions in a sloping soil  
997 lysimeter with time-varying flow paths: Direct observation of internal and external transport  
998 variability. *Water Resources Research*, 52(9), 7105–7129.  
999 <https://doi.org/10.1002/2016WR018620>
- 1000 Kim, M., Volkmann, T. H., Harman, C., Wang, Y., Troch, P. A. Direct observation of hillslope  
1001 scale StorAge Selection functions in an experimental hydrologic system: Geomorphologic  
1002 structure and the preferential discharge of old water. Under review at Water Resources  
1003 Research. Preprint: <https://www.essoar.org/doi/10.1002/essoar.10504485.1>
- 1004 Koestel, J., Kemna, A., Javaux, M., Binley, A., & Vereecken, H. (2008). Quantitative imaging of  
1005 solute transport in an unsaturated and undisturbed soil monolith with 3-D ERT and TDR.  
1006 *Water Resources Research*, 44(12), 1–17. <https://doi.org/10.1029/2007WR006755>
- 1007 Kuppel, S., Tetzlaff, D., Maneta, M. P., & Soulsby, C. (2020). Critical zonenstorage controls on  
1008 the water ages of ecohydrological outputs. *Geophysical Research Letters*, 47,  
1009 e2020GL088897. <https://doi.org/10.1029/2020GL088897>
- 1010 LaBrecque, D. J., and X. Yang (2001), Difference inversion of ERT data: A fast inversion  
1011 method for 3-D in situ monitoring, *J. Environ. Eng. Geophys.*, 6, 83-89.  
1012 <https://doi.org/10.4133/JEEG6.2.83>
- 1013 Landon, M. K., Delin, G. N., Komor, S. C., & Regan, C. P. (2000). Relation of Pathways and  
1014 Transit Times of Recharge Water to Nitrate Concentrations Using Stable Isotopes.  
1015 *Groundwater*, 38(3), 381–395.
- 1016 Looms, M. C., Jensen, K. H., Binley, A., & Nielsen, L. (2008). Monitoring Unsaturated Flow  
1017 and Transport Using Cross-Borehole Geophysical Methods. *Vadose Zone Journal*, 7(1),  
1018 227. <https://doi.org/10.2136/vzj2006.0129>

- 1019 Maher, K. (2010). The dependence of chemical weathering rates on fluid residence time. *Earth*  
1020 *and Planetary Science Letters*, 294(1–2), 101–110.  
1021 <https://doi.org/10.1016/j.epsl.2010.03.010>
- 1022 Maher, K. (2011). The role of fluid residence time and topographic scales in determining  
1023 chemical fluxes from landscapes. *Earth and Planetary Science Letters*, 312(1–2), 48–58.  
1024 <https://doi.org/10.1016/j.epsl.2011.09.040>
- 1025 Małoszewski, P., & Zuber, A. (1982). Determining the turnover time of groundwater systems  
1026 with the aid of environmental tracers. *Journal of Hydrology*, 57, 207–231.  
1027 [https://doi.org/10.1016/0022-1694\(82\)90147-0](https://doi.org/10.1016/0022-1694(82)90147-0)
- 1028 McDonnell, J. J., McGuire, K., Aggarwal, P., Beven, K. J., Biondi, D., Destouni, G., ... Wrede,  
1029 S. (2010). How old is streamwater? Open questions in catchment transit time  
1030 conceptualization, modelling and analysis. *Hydrological Processes*, 24, 1745–1754.  
1031 <https://doi.org/10.1002/hyp.7796>
- 1032 McGuire, K. J., & McDonnell, J. J. (2006). A review and evaluation of catchment transit time  
1033 modeling. *Journal of Hydrology*, 330, 543–563.  
1034 <https://doi.org/10.1016/j.jhydrol.2006.04.020>
- 1035 Niemi, A. J. (1977), Residence time distributions of variable flow processes, *Int. J. Appl. Radiat.*  
1036 *Isotopes*, 28(10–1), 855–860, doi:10.1016/0020-708X(77)90026-6
- 1037 Pangle, L. a., DeLong, S. B., Abramson, N., Adams, J., Barron-Gafford, G. a., Breshears, D. D.,  
1038 ... Zeng, X. (2015). The Landscape Evolution Observatory: A large-scale controllable  
1039 infrastructure to study coupled Earth-surface processes. *Geomorphology*, 1–14.  
1040 <https://doi.org/10.1016/j.geomorph.2015.01.020>
- 1041 Pangle, L. A., Kim, M., Cardoso, C., Lora, M., Meira Neto, A. A., Volkmann, T. H. M., ...  
1042 Harman, C. J. (2017). The mechanistic basis for storage-dependent age distributions of  
1043 water discharged from an experimental hillslope. *Water Resources Research*, 53(4), 2733–  
1044 2754. <https://doi.org/10.1002/2016WR019901>

- 1045 Perri, M. T., Cassiani, G., Gervasio, I., Deiana, R., & Binley, A. (2012). A saline tracer test  
1046 monitored via both surface and cross-borehole electrical resistivity tomography:  
1047 Comparison of time-lapse results. *Journal of Applied Geophysics*, 79, 6–16.  
1048 <https://doi.org/10.1016/j.jappgeo.2011.12.011>
- 1049 Pohlmann, M., Dontsova, K., Root, R., Ruiz, J., Troch, P., & Chorover, J. (2016). Pore water  
1050 chemistry reveals gradients in mineral transformation across a model basaltic hillslope.  
1051 *Geochemistry, Geophysics, Geosystems*, 17(6), 2054–2069.  
1052 <https://doi.org/10.1002/2016GC006270>
- 1053 Porporato, A., & Calabrese, S. (2015). On the probabilistic structure of water age. *Water*  
1054 *Resources Research*, 51(5), 3588–3600. <https://doi.org/10.1002/2015WR017027>
- 1055 Rinaldo, A., Benettin, P., Harman, C. J., Hrachowitz, M., McGuire, K. J., Velde, Y. Van Der, ...  
1056 Botter, G. (2015). Storage selection functions: A coherent framework for quantifying how  
1057 catchments store and release water and solutes. *Water Resources Research*, 51, 1–8.  
1058 <https://doi.org/10.1002/2015WR017273>.Received
- 1059 Rodriguez, N. B., McGuire, K. J., & Klaus, J. (2018). Time-Varying Storage–Water Age  
1060 Relationships in a Catchment With a Mediterranean Climate. *Water Resources Research*,  
1061 54(6), 3988–4008. <https://doi.org/10.1029/2017WR021964>
- 1062 Sengupta, A., Wang, Y., Meira Neto, A. A., Matos, K. A., Dontsova, K., Root, R., ... & Troch, P.  
1063 A. (2016). Soil lysimeter excavation for coupled hydrological, geochemical, and  
1064 microbiological investigations. *Journal of Visualized Experiments*, 115, 1-11.
- 1065 Singha, K., & Gorelick, S. M. (2006). Hydrogeophysical tracking of three-dimensional tracer  
1066 migration: The concept and application of apparent petrophysical relations. *Water*  
1067 *Resources Research*, 42(6), 1–14. <https://doi.org/10.1029/2005WR004568>
- 1068 Slater, L., Binley, a., Versteeg, R., Cassiani, G., Birken, R., & Sandberg, S. (2001). A 3D ERT  
1069 study of solute transport in a large experimental tank. *Journal of Applied Geophysics*, 49,  
1070 211–229. [https://doi.org/10.1016/S0926-9851\(02\)00124-6](https://doi.org/10.1016/S0926-9851(02)00124-6)

- 1071 Slater, L., Binley, A. M., Daily, W., & Johnson, R. (2000). Cross-hole electrical imaging of a  
1072 controlled saline tracer injection. *Journal of Applied Geophysics*, 44(2–3), 85–102.
- 1073 Sprenger, M., Stumpp, C., Weiler, M., Aeschbach, W., Allen, S. T., Benettin, P., et al. (2019).  
1074 The demographics of water: A review of water ages in the critical zone. *Reviews of*  
1075 *Geophysics*, 57. <https://doi.org/10.1029/2018RG000633>
- 1076 Turner, J., Albrechtsen, H. J., Bonell, M., Duguet, J. P., Harris, B., Meckenstock, R., ... van  
1077 Lanen, H. (2006). Future trends in transport and fate of diffuse contaminants in catchments,  
1078 with special emphasis on stable isotope applications. *Hydrological Processes*, 20(1), 205–  
1079 213. <https://doi.org/10.1002/hyp.6074>
- 1080 Van Der Velde, Y., Torfs, P. J. J. F., Van Der Zee, S. E. A. T. M., & Uijlenhoet, R. (2012).  
1081 Quantifying catchment-scale mixing and its effect on time-varying travel time distributions.  
1082 *Water Resources Research*, 48(6), 1–13. <https://doi.org/10.1029/2011WR011310>
- 1083 van der Velde, Y., Heidbüchel, I., Lyon, S. W., Nyberg, L., Rodhe, A., Bishop, K., & Troch, P.  
1084 a. (2015). Consequences of mixing assumptions for time-variable travel time distributions.  
1085 *Hydrological Processes*, 29(16), 3460–3474. <https://doi.org/10.1002/hyp.10372>
- 1086 Wherer, M., & Slater, L. D. (2014). Characterization of water content dynamics and tracer  
1087 breakthrough by 3-D electrical resistivity tomography (ERT) under transient unsaturated  
1088 conditions. *Water Resources Research*, 50(7), 5510–5531.  
1089 <https://doi.org/10.1002/2013WR014910>.Received
- 1090 Wilusz, D. C., Harman, C. J., & Ball, W. P. (2017). Sensitivity of Catchment Transit Times to  
1091 Rainfall Variability Under Present and Future Climates. *Water Resources Research*, 53(12),  
1092 10231–10256. <https://doi.org/10.1002/2017WR020894>
- 1093 Wilusz, D. C., Harman, C. J., Ball, W. P., Maxwell, R. M., & Buda, A. R. (2020). Using particle  
1094 tracking to understand flow paths, age distributions, and the paradoxical origins of the  
1095 inverse storage effect in an experimental catchment. *Water Resources Research*, 56,  
1096 e2019WR025140. <https://doi.org/10.1029/2019WR025140>

- 1097 Yang, J., Heidbüchel, I., Musolff, A., Reinstorf, F., & Fleckenstein, J. H. (2018). Exploring the  
1098 Dynamics of Transit Times and Subsurface Mixing in a Small Agricultural Catchment.